Diverse dynamics of glutamatergic input underlie heterogeneous response patterns of olfactory bulb outputs *in vivo*

Andrew K. Moran[1,2], Thomas P. Eiting[2], Matt Wachowiak[2]

[1]Interdepartmental Program in Neuroscience, [2]Department of Neurobiology and Anatomy, University of Utah School of Medicine, Salt Lake City, UT

Correspondence: Matt Wachowiak, Department of Neurobiology and Anatomy, University of Utah, Salt Lake City, UT, USA. email: matt.wachowiak@utah.edu

ABSTRACT

Mitral/tufted (MT) cells of the olfactory bulb (OB) show diverse temporal responses to odorant stimulation that are thought to encode odor information. To understand the role of sensory input dynamics versus OB circuit mechanisms in generating this diversity, we imaged glutamate signaling onto MT cell dendrites in anesthetized and awake mice. We found surprising diversity in the dynamics of these signals, including excitatory, suppressive, and biphasic responses as well as nonlinear changes in glutamate over multiple inhalations. Glutamate response patterns persisted after blockade of postsynaptic activity, implicating sensory neurons as the primary source of glutamate signaling onto MT cells. Simultaneous imaging of glutamate and calcium signals from MT cell dendrites revealed highly correlated responses for both signals. Thus, the dynamics of sensory input alone, rather than emergent features of OB circuits, may account for much of the diversity in MT cell responses that underlies odor representations at this stage.

Keywords: imaging, glutamate, calcium, temporal coding, active sensing

INTRODUCTION

The neural activity underlying odor perception is inherently dynamic. In vertebrates, olfactory sensory input arrives at the brain as bursts of activity driven by each inhalation, and patterns of inhalation are actively controlled by an animal as it samples its environment. At the level of the olfactory bulb (OB), olfactory sensory neurons (OSNs) expressing a single type of odorant receptor converge onto discrete glomeruli (Ressler et al., 1994; Vassar et al., 1994), where they make excitatory, glutamatergic synapses onto an array of targets including juxtaglomerular interneurons and the principal OB output neurons, mitral and tufted (MT) cells (Wachowiak and Shipley, 2006). Odorant responses among MT cells can be temporally complex, including sequences of excitation and suppression that occur relative to a single inhalation of odorant and across multiple inhalations, or sniffs (Chaput, 1986; Shusterman et al., 2011; Patterson et al., 2013; Diaz-Quesada et al., 2018). There is strong evidence that olfactory information is represented both by the identity of activated MT cells as well as by their temporal dynamics (Chaput, 1986; Schaefer and Margrie, 2007; Junek et al., 2010; Wilson et al., 2017; Li et al., 2019).

Much of the complexity in response patterns of MT cells has been attributed to processing by OB circuits – in particular, inhibitory circuits that target the apical or lateral MT cell dendrites (Yokoi et al., 1995; Schoppa and Urban, 2003; Gire and Schoppa, 2009; Shao et al., 2012; Geramita and Urban, 2017). Intrinsic properties of MT cells have also been proposed to contribute to diversity in MT cell temporal responses to odors (Padmanabhan and Urban, 2010). However, excitatory synaptic inputs to MT cells, which occur solely on the MT cell apical tuft in each glomerulus, may also contribute to generating temporally complex and diverse patterns of MT cell spiking. OSN inputs themselves respond to odorant inhalation with different response latencies and show nonlinear changes in their activation patterns as a function of odorant concentration, sampling time and sampling frequency (McGann et al., 2005; Spors et al., 2006; Verhagen et al., 2007). Additional diversity in excitatory synaptic input to MT cells can arise from external tufted (ET) cells, a glutamatergic interneuron that is a major source of excitatory drive in the glomerulus (Hayar et al., 2004; De Saint Jan et al., 2009; Gire et al., 2012; Gire et al., 2019). ET cells constitute a control point

by which inhibitory circuits can regulate MT cell excitation by gating ET cell activation (Gire and Schoppa, 2009; Banerjee et al., 2015). Thus, diversity in the strength and timing of glutamatergic input to MT cells, in addition to inhibitory inputs, may be a major contributor to the dynamics of MT cell spiking that are thought to be important in encoding odor information. However, the contribution of glutamatergic input dynamics to MT cell odorant response patterns *in vivo* remains poorly understood.

Here, we imaged odorant-evoked and inhalation-linked glutamate signals in glomeruli of the mouse OB using the genetically-encoded glutamate sensor iGluSnFR and its second-generation 'SF' variants (Marvin et al., 2013; Marvin et al., 2018), expressed selectively in MT cells. iGluSnFR and the SF-iGluSnFRs reported glutamate signals that were confined to the glomerular neuropil and MT cell lateral dendrites, where MT cells release glutamate. We also directly compared presynaptic, glutamatergic input and postsynaptic activation of MT cells using simultaneous, dual-color imaging of glutamate and calcium signals from MT cells in the same glomerulus. Glomerular glutamate transients were tightly coupled to inhalation and reported inhalation-linked dynamics with high signal-to-noise ratio and a higher temporal fidelity than calcium-sensitive reporters, allowing temporally precise monitoring of glutamatergic signaling across the dorsal OB on a single-trial basis and in both the anesthetized and awake mouse. Overall, we observed a surprising high degree of diversity in the temporal dynamics of glutamatergic input onto the apical tufts of MT cells in a glomerulus, over time scales involving a single inhalation and across multiple inhalations of odorant. Pharmacological experiments suggested that these diverse temporal patterns are largely mediated directly by OSNs. Finally, we found a high correspondence between the dynamics of glutamatergic input and that of MT cell output across glomeruli. Our results reveal remarkable diversity in the dynamics of excitatory input to MT cells and suggest that the complex spatiotemporal activity patterns thought to play a critical role in coding odor information at this stage may arise largely from feedforward excitatory pathways. Our results also highlight the utility of glutamate imaging for dissecting OB circuit organization and function in vivo.

RESULTS

Imaging glutamate signaling across mitral/tufted cell dendrites

We first performed a basic characterization of sensory-evoked glutamate signals reported by iGluSnFR (Marvin et al., 2013) and its second-generation variants, which have a range of affinities for glutamate (Marvin et al., 2018). iGluSnFR expression was targeted to MT cells using Cre-dependent viral vectors injected into the OB of Pcdh21-Cre or Tbet-Cre transgenic mice. All iGluSnFR variants showed expression that appeared enriched on the membrane surface and which spanned all cellular compartments (Figure 1A). When imaged in vivo with two-photon laser scanning microscopy targeted to the glomerular layer, resting fluorescence showed clearly-delineated glomeruli, as expected from expression across MT cell apical dendrites (Figure 1B).

We have previously shown, using the first-generation iGluSnFR, that each inhalation of odorant drives a transient of glutamate release onto juxtaglomerular interneuron processes in the glomerular neuropil (Brunert et al., 2016)**.** We observed similar glutamate signals with iGluSnFRs expressed in MT cells (Figure 1B, top). A striking feature of these signals was the considerable diversity in the dynamics of odorant- and inhalation-evoked glutamate transients, with different glomeruli showing glutamate transients with varying onset latencies and durations, and with distinct changes in the glutamate signal evoked by successive inhalations across a longer odorant presentation (Figure 1B, bottom). Before investigating this diversity further, we more fully characterized sensory-evoked glutamate signals as reported by the three second-generation SF-iGluSnFR variants, which have varying affinities for glutamate: A184S (reported K_d, 7 μM), A184V (K_d, 40 μM) and S72A (K_d, 200 μM) (Marvin et al., 2018).

We first compared inhalation-linked dynamics of glutamate signals by generating 'inhalation-triggered' average responses (ITAs) from multiple inhalations at low (0.25 - 0.5 Hz) frequency, as we have done previously (Diaz-Quesada et al., 2018; Short and Wachowiak, 2019). We compared ITAs generated across multiple glomerulus-odor pairs using the three SF variants. Each variant tracked single inhalation responses with high fidelity**.** SF-iGluSnFR variants showed response amplitudes to odorant inhalation that increased with their reported affinity (Figure 1C, left), with maximal response

amplitudes (90th percentile of max ΔF/F across all glomerulus-odor pairs) of 59% for S72A (n = 18 glomerulus-odor pairs, 2 mice); 74% for A184V (n = 117, 2 mice); and 104% for A184S (n = 438, 5 mice).

In terms of inhalation-linked glutamate dynamics, most ITA transients consisted of a simple waveform with a rapid rise and a return to baseline fluorescence that was well-fit by a single exponential decay. In a few cases, ITA transients were more complex, for example including a 'shoulder' component resulting in a longer-duration glutamate signal (not shown). For the majority-case simple ITA transients, the shortest decay time following each inhalation (25th percentile across all glomerulus-odor pairs) varied according to SF-iGluSnFR affinity, ranging from 120 msec for S72A (n = 18 glomerulus-odor pairs from 2 mice), 162 msec for A184V (n=91, 2 mice) and 297 msec for A184S (n=370, 5 mice). However, across all glomerulus-odor pairs, decay times varied for different glomerulus-odor combinations and the range of decay times overlapped subtantially across the three variants (Figure 1C, right). This variability and overlap suggests, at least for the medium and high-affinity SF-iGluSnFRs, that variation in the dynamics of the SF-iGluSnFR signal imaged from MT cell apical tufts is largely indicative of the variable dynamics of glutamate signalling in the glomerulus, as opposed to intrinsic kinetic differences of the reporter.

We next characterized glutamate signals reported from different MT cell compartments. The apical dendritic tuft within the glomerulus is the only confirmed site of glutamatergic input to MT cells (Schoppa and Urban, 2003); however, MT cells also release glutamate from dendrodendritic synapses on their apical tuft and lateral dendrites (Isaacson and Strowbridge, 1998; Isaacson, 1999), and synaptic contacts are present along the mitral cell primary dendrite (Matsuno et al., 2017). To assess glutamate signaling across the MT cell dendritic field, we used the high-affinity A184S variant and imaged at high optical zoom from the apical tufts, distal primary dendrites, and lateral dendrites. In the superficial OB, odorant-evoked glutamate signals appeared restricted to MT cell apical tufts of responsive glomeruli (Figure 1D). While SF-iGluSnFR expression was apparent along the length of the MT cell apical dendrite as it entered a glomerulus, evoked glutamate signals were negligible outside of the glomerulus (Figure 1D, E). Likewise, glutamate signals were not apparent on MT cell somata (Figure 1D,

E).

Using A184S to image from the external plexiform layer (EPL), odorant stimulation elicited smaller-magnitude glutamate signals along MT cell lateral dendrites, with different odorants evoking signals in different subsets of lateral dendrites (Figure 1F). Since MT cells are not thought to receive glutamatergic input via their lateral dendrites (Schoppa and Urban, 2003; Wachowiak and Shipley, 2006) we interpret these signals as reflecting glutamate release from the same cells in which the reporter is expressed. Glutamate signals appeared continuous along the length of a lateral dendrite, although we did not attempt to image at a high enough zoom to resolve potentially localized release sites, and spines are not present on MT cell lateral dendrites. Some dendrites appeared to show weak odorant-evoked fluorescence decreases, suggesting a decrease in ongoing release associated with odorant stimulation (Figure 1F, ROIs 2 and 4). Taken together, these data indicate that SF-iGluSnFRs report glutamatergic input to MT cell apical dendrites with high sensitivity, and can also report glutamate release from MT cell lateral dendrites.

Diverse temporal patterns of glutamatergic signaling across multiple time scales

The timing of odorant- and inhalation-evoked MT cell spiking varies across MT cells and across odorants, and has long been hypothesized to play a role in coding odor information (Chaput, 1986; Schaefer and Margrie, 2007; Junek et al., 2010; Wilson et al., 2017). To assess the degree to which variability is present at the level of glutamatergic input to the cohort of MT cells innervating a glomerulus, we analyzed inhalation-linked dynamics of the glutamate signal across glomerulus-odor pairs. We first analyzed ITAs derived from low-frequency (0.25 Hz) inhalations imaged with SF-iGluSnFR.A184S and A184V. While odorants evoked distinct combinatorial patterns of glutamate signals across glomeruli, as expected (Figure 2A), they also elicited inhalation-triggered dynamics that varied substantially across glomeruli and odorants (Figure 2B). Glomeruli activated by the same odorant could show ITA waveforms with different onset latencies, rise-times, and durations, and the same glomerulus could show distinct ITA dynamics for different odorants (Figure 2B). Across all glomeruli imaged with A184S (n = 431 glomerulus-odor pairs, 5 mice), ITA onset latencies ranged

from 113 to 253 msec (10th - 90th percentiles), time to ITA peak ranged from 300 to 533 msec, and ITA durations ranged from 360 to 867 msec (Figure 2C). Notably, inhalation also occasionally elicited fluorescence decreases in a glomerulus, suggesting a phasic decrease in ongoing glutamate release (Figure 2B, see ROI 6), although this was rare. Responses using the A184V variant were similar, with onset latencies ranging from 153 to 313 msec (10th - 90th percentiles, 113 pairs from 3 mice), time to peak ranging from 313 to 727 msec, and ITA durations ranging from 260 to 1100 msec. Thus, the dynamics of glutamatergic input onto MT cells spans a wide range and can vary substantially depending on both glomerular and odorant identity.

We have previously reported similar variability in inhalation-linked dynamics of OSNs themselves, as reflected in calcium signals imaged from OSN presynaptic terminals (Spors et al., 2006; Short and Wachowiak, 2019). We thus compared the variability seen in the glutamate ITA with that from OSNs expressing the genetically-encoded reporter GCaMP6f, in response to the same odorants in separate mice (Figure 2D). ITA onset latencies for OSN inputs to glomeruli were, as a population, longer than those for SF-iGluSnFR (OSNs/GCaMP6f: 298 ± 110 msec (mean ± SD, n = 91 glomerulus odor pairs, 6 mice, MTs/iGluSnFR A184S: 188 ± 60 msec, n = 438 glomerulus-odor pairs, 7 mice, Mann-Whitney Test, $p = 8 \times 10^{-23}$), reflecting the slower response time of GCaMP6f compared to iGluSnFR (Richter et al., 2018). These results match those obtained in a separate study from our laboratory (Short and Wachowiak, 2019), which found GCaMP6f ITA onset latencies of 268 ± 100 msec. Despite the slower response of the GCaMP6f signals, the range of ITA latencies after subtracting the median latency for each was highly overlapping (Figure 2D). These results suggest that variability in the onset times of glutamate transients onto MT cell after each inhalation might largely reflect variability in the timing of spike bursts arriving at OSN presynaptic terminals.

Diversity of glutamatergic signaling across multiple inhalations.

To more fully investigate the temporal diversity in patterns of glutamate signaling onto MT cells, we imaged responses across the dorsal OB to 23 odorants (plus one 'blank' control), using a novel olfactometer design that allows rapid presentation of

successive odorants with minimal possibility of cross-contamination (Burton et al., 2019). Odorants were presented for 2 sec using an artificial inhalation rate of 3 Hz, and delivered at relatively low concentrations across for most odorants (see Table 1) such that each odorant evoked relatively sparse responses across the field of imaged glomeruli (Figure 3A). 16.5% of all glomerulus-odor pairs (748/4520; 7 fields of view from 3 mice) showed responses that were significant according to a highly conservative criterion (± 7 SD from baseline, ~ 1% false positive rate, see Methods) for an odorant-evoked change in SF-iGluSnFR fluorescence. Responsive glomeruli were narrowly tuned across the 23-odorant panel, with high values of lifetime sparseness (Schlief and Wilson, 2007) for excited glomeruli (S = 0.91 ± 0.05 (mean ± SD)).

We observed considerable diversity in the temporal patterns of odorant-evoked glutamate signals. Patterns were robust, occurring consistently over repeated presentations (Figure 3B). The most common response pattern consisted of inhalation-linked transients that were consistent over the 2-sec presentation and returned rapidly to baseline at the end of presentation (Figure 3C, e.g., isopropyl tiglate). However, other excitatory response patterns were common, including transient increases occurring immediately after odorant onset and not following any subsequent sniff, prolonged increases that returned slowly to baseline after odorant offset, and slow rises in glutamate over the 2-sec presentation (Figure 3C, e.g. hexanoic acid). Response patterns varied for different glomeruli activated by the same odorant and for responses of the same glomerulus to different odorants (Figure 3C, e.g., valeric acid, heptanal, isopropyl tiglate, green trace), indicating that response patterns were neither a function of SF-iGluSnFR expression levels in a particular glomerulus nor a function of any particular odorant.

Notably, odorants also could evoke responses with a strong suppressive component, either following an initial transient increase in glutamate or consisting solely of fluorescence decreases (Figure 3D, E). Suppressive responses to odorants were rare but clearly apparent even in single trials (e.g., Figure 3B, ROI 4), with pure suppression seen in 7.2% (54/748) of glomerulus-odor pairs and biphasic (excitatory and suppressed) responses, seen in 3.5% (26/748) of pairs (Figure 3E).

One consequence of this diversity was that the relative magnitude of

glutamatergic signaling in different glomeruli—and thus the glomerular representation of an odorant—varied over the 2-sec odor presentation. To quantify this, we generated vectors consisting of time-binned glutamate signals (bin width, 387 msec) across all glomeruli in a field of view, beginning 150 msec after odorant onset, and correlated the vector in the first time bin with that from each successive time bin over the 2-s odor presentation. Among all glomerulus-odor pairs, there was a substantial decrease in correlation beginning in the second bin (time bin 2 vs. time bin 1: $r = 0.52 \pm 0.32$) and continuing to the last bin (time bin 5 vs. time bin 1: $r = 0.39 \pm 0.37$), although the degree of decorrelation varied greatly for different odorants (Figure 3F). For example, as seen in Figure 3C (insets), responses to some odorants decorrelated substantially after the initial response (Figure 3C, e.g., hexanoic acid, heptanal) while responses to other odorants remained consistent (Figure 3C, e.g., isopropyl tiglate). This decorrelation is qualitatively similar to that observed in patterns of MT cell spiking over repeated samples of odorant (Patterson et al., 2013; Diaz-Quesada et al., 2018), suggesting that time-dependent decorrelation can arise at the level of glutamatergic input to MT cells.

Odorant concentration systematically alters the dynamics of glomerular glutamate signals

Distinct temporal patterns of glutamatergic signaling might be determined by the strength of odorant stimulation for a given glomerulus, relative to the dynamic range of that glomerulus for the odorant. Different temporal patterns might arise by inducing rapid adaptation or sustained responses (Lecoq et al., 2009; Matsumoto et al., 2009). To address this, we investigated the effect of odorant concentration on glutamatergic input by presenting a smaller number of odorants (3 – 5 per experiment, n = 4 mice) at 3 concentrations spanning a 10-fold range (Table 1), using 2 Hz inhalations and a 4-sec odorant presentation. These experiments used first-generation iGluSnFR (Marvin et al., 2013) expressed in MT cells of Pcd-Cre mice. Changing concentration often dramatically altered the dynamics of the glutamate response over the time of the presentation (Figure 4A). In many glomerulus-odor pairs, odorants evoked consistent inhalation-driven transients throughout odorant presentation at the lowest (1x) concentration, which changed to highly adapting responses at higher concentrations

(Figure 4A, e.g., methyl valerate, ethyl tiglate). In other glomeruli (even for the same odorants), increasing concentration appeared to recruit glutamate signals with repeated inhalations over the course of the presentation; this often included an increase in the tonic component of the glutamate signal (Figure 4A, e.g., methyl valerate). Other glomerulus-odor pairs showed little adaptation and little effect of concentration (Figure 4A, e.g., 2-hexanone).

To quantify these changes along a particular dimension of response pattern, we calculated the normalized change in response amplitude from the beginning to the end of odorant presentation, as T_2-T_1/T_{max} across 189 glomerulus-odor pairs (Figure 4B). With this measure, negative values indicate adaptation while positive values indicate facilitation. There was a high degree of variability in changes in glutamate signal over time (Figure 4B), although adaptation was more common across the population, with significantly negative values across all glomerulus-odor pairs (n=189 G-O pairs, mean ± SD, One sample t-test, 1x: -0.19 ± 0.35, p = 2. x10-12, 3x: -0.14 ± 0.40, p = 5 x 10-6, 10x : -0.26 ± 0.44, p = 8 x 10-14). There was slightly but significantly more adaptation at the highest concentration (10x) compared to the lowest (1x) (paired t-test, p=0.044).

A second effect of increasing odorant concentration was a reduction in the degree to which glutamate signaling was modulated by each inhalation, with inhalation-linked transients in many glomeruli being replaced by a tonic glutamate signal (Figure 4A, e.g., methyl valerate, ethyl tiglate). We quantified this effect by measuring the coherence of the iGluSnFR signal relative to a simulated 2 Hz inhalation pulse. Across all glomerulus-odorant pairs, coherence with inhalation decreased with increasing concentration (Figure 4C) (mean ± SD, 1x: 0.86 ± 0.16, 3x: 0.75 ± 0.28, 10x: 0.56 ± 0.32, one-way ANOVA, $F_{3,552} = 2.54$, $p < 0.001$). Notably, however, this effect varied depending on the odorant used (two-way ANOVA, concentration x odorant: $F_{8,552} = 3.87$, $p = 2.0 \times 10^{-4}$), with glomeruli responsive to the ketone 2-hexanone showing no loss of inhalation-linked coherence as concentration increased, while glomeruli responsive to the other tested odorants (all esters) showed a substantial loss of coherence (Figure 4D). These odorant-specific differences may reflect differences in the kinetics of odorant sorption or clearance from the nasal epithelium, although further experiments with a more diverse odorant panel are necessary to resolve this question.

Overall, these results indicate that odorant concentration has systematic impacts on the dynamics of glutamatergic signaling onto MT cells, with a slight increase in adaptation and a substantial decrease in inhalation coupling as odorant concentration increases.

Limited contribution of postsynaptic circuitry to diverse glutamate signaling onto MT cells

Sensory-evoked glutamatergic input onto MT cells can arise from two main sources: OSNs themselves and external tufted (ET) cells, with the latter constituting a feedforward disynaptic excitatory pathway for MT cell excitation (Hayar et al., 2004; De Saint Jan et al., 2009; Gire et al., 2012; Vaaga and Westbrook, 2016). The relative contribution of OSN versus ET cell-mediated glutamatergic signaling to odor-evoked responses of MT cells remains unclear. In addition, glomerular glutamate signals may arise from glutamate release by MT cell dendrites (Isaacson, 1999; Najac et al., 2015), and thus at least partially reflect MT cell excitation rather than simply presynaptic MT cell inputs. To disambiguate some of these sources, we compared odor-evoked glutamate dynamics before and after pharmacological blockade of postsynaptic activity with ionotropic glutamate receptor antagonists (2 mM/1 mM APV/NBQX, applied to the dorsal OB surface), as done previously (Gurden et al., 2006; Pírez and Wachowiak, 2008; Lecoq et al., 2009). Because iGluSnFR and SF-iGluSnFR are derived from a bacterial glutamate transporter and not from glutamate receptors, ionotropic glutamate receptor antagonists do not impact binding of glutamate to iGluSnFR (Marvin et al., 2013). We reasoned that this approach would largely prevent OSN-driven excitation of ET cells, MT cells and also periglomerular or short axon cells, and thus allow us to image evoked MT cell glutamate signals arising solely from OSN inputs.

We used a 12-odorant panel and 3 Hz artificial inhalation to acquire diverse temporal patterns of glutamate responses in dorsal glomeruli, as described above. This approach yielded significant odorant responses in 83 glomerulus-odorant pairs across 3 mice, and included the range of excitatory response patterns described earlier (Figure 5A-C). Surprisingly, APV/NBQX had little overall impact on the magnitude of evoked iGluSnFR signals: while there was some variability in the effect for particular glomerulus-odor pairs, neither mean nor peak excitatory response magnitudes showed

a significant overall change after APV/NBQX application (paired t-tests, p = 0.147 for mean amplitude, p = 0.605 for peak amplitude) (Figure 5D).

APV/NBQX did, however, impact the temporal dynamics of the glutamate signal for a subset of responses. In particular, APV/NBQX affected transient response patterns, either by reducing the rapid adaptation that occurred following the initial inhalation of odorant or by enhancing longer-lasting, tonic-type responses (Figure 5B, C). This was reflected as a reduction in T_2-T_1/T_{max} values by APV/NBQX, with significant reductions seen in each of three mice (Figure 5D), (paired t-tests, mouse 1, n= 7 glomerulus-odor pairs, p=0.001; mouse 2: n = 34, p=0.001; mouse 3: n = 42, p=5.45 x 10^{-6}). Other response dynamics appeared unaffected by glutamate receptor blockade: inhalation-linked responses persisted in the presence of APV/NBQX, as did slowly-increasing response patterns in particular glomeruli (Figure 5B). Overall, while these results indicate that postsynaptic circuitry plays some role in temporally sharpening excitation of MT cells across multiple samples of odorant, they also suggest that the bulk of odor-evoked glutamatergic input to MT cells arises from OSNs, and that this source alone can account for much of the temporal diversity in glutamatergic signaling seen across OB glomeruli.

Glomerular glutamate signaling shows diverse temporal dynamics in awake mice

To assess diversity in glutamate signaling onto MT cells during natural odor sampling, we imaged iGluSnFR signals from dorsal glomeruli in awake, head-fixed mice, while monitoring nasal airflow with an external sensor. Respiration frequencies were typically between 3 and 6 Hz (mean frequency per session, 4.4 ± 0.34 Hz, 5 sessions), with occasional pauses and bouts of higher-frequency sniffing. Glutamate transients in awake mice were temporally diverse, similar to anesthetized mice. For many glomeruli, each inhalation at 'resting' frequencies (defined as below 5 Hz) elicited a clear glutamate transient (Figure 6A, 6B). We measured inhalation-linked dynamics for glomerulus-odorant pairs showing significant respiratory modulation by constructing ITA waveforms as done with artificial inhalation, but using the external flow sensor to determine inhalation timing. ITA waveforms generated from these data were approximately sinusoidal (Figure 6A, lower right), allowing for straightforward estimates

of onset latency and time-to-peak of the glutamate signal relative to inhalation.

ITA onset latencies relative to the start of inhalation, compiled from two mice (10 odorants, 3 fields of view, 70 glomerulus-odorant pairs), ranged from 40 - 150 msec (mean ± SD; 74 ± 29 msec), with peak latencies (time from inhalation start to ITA peak) ranging from 140 - 300 msec (mean ± SD; 184 ± 37 msec) (Figure 6B). As seen with artificial inhalation, these dynamics could vary across glomeruli and odorants: for example, glomeruli in the same field of view activated by ethyl butyrate showed latencies ranging from 93 – 153 msec. These latency differences were apparent in single trials and were consistent across repeated inhalations of odorant (Figure 6A). However, for many odorants, there was much less variation in ITA latencies across glomeruli in a given field of view; overall, for 10 unique odor-FOVs tested in 2 mice, the variation in onset latencies across all glomeruli in the same field of view ranged from 7 – 60 msec, whereas the time to peak ranged from 7 – 100 msec (Figure 6B).

There was also variability in the degree of coupling of iGluSnFR signals to respiration: for many glomerulus-odorant pairs, glutamate signals were not clearly modulated by respiration but instead consisted of a tonic glutamate increase. The same glomerulus could show strong coupling to respiration for one odorant (Figure 6C, left) and a complete lack of respiratory coupling for another odorant (Figure 6C, right), and different glomeruli responsive to the same odorant could show either strong or no respiratory coupling (Figure 6D, bottom two traces), indicating that the lack of coupling was not due to differences in sniffing or inhalation from trial to trial, nor was it due to differences in odorant stimulus profile. Glomeruli could also show odorant-specific fluorescence decreases (Figure 6D, top trace).

Glutamate signals also showed diverse odorant responses over multiple inhalations. As with artificial inhalation, the evolution of responses over several seconds of odorant presentation included slow increases in tonic glutamate and adaptation of inhalation-linked and tonic glutamate signals (Figures 6C, D,). We also observed concentration-dependent changes in glutamate dynamics, with increasing odorant concentrations leading to stronger adaptation of glutamate signal for strongly-responsive glomeruli and recruitment of slowly-increasing responses in weakly-responsive glomeruli (Figure 6E). As with artificial inhalation data, such changes

resulted in an evolution of the relative patterns of glutamatergic signals across glomeruli that developed over repeated samples of odorant, and glutamate response patterns decorrelated more substantially for some odorants than others (Figure 6F). Overall, these data indicate that the diversity in dynamics of glutamatergic inputs to MT cells that we observed with artificial inhalation under anesthesia is also present in awake mice.

Correspondence between dynamics of glutamatergic inputs and MT cell postsynaptic activity.

While glutamatergic signaling in the glomerulus is the sole source of excitatory input to MT cells, multiple inhibitory circuits are thought to shape patterns of MT cell excitation (Schoppa and Urban, 2003; Wachowiak and Shipley, 2006; Gire and Schoppa, 2009; Burton, 2017). Because MT cell spikes back-propagate along the MT cell apical dendrite and invade the apical tuft (Bischofberger and Jonas, 1997; Chen et al., 1997), calcium signals imaged from the tuft provide a proxy for patterns of MT cell spike output from each glomerulus (Charpak et al., 2001; Economo et al., 2016). Thus, to gain insight into the relative contributions of excitatory versus inhibitory inputs to MT cell response patterns, we compared glutamate signals with calcium signals measured from MT cell apical dendrites of the same glomerulus, imaged simultaneously. To achieve this, we co-expressed SF-iGluSnFR.A184S and the red calcium reporter jRGECO1a (Dana et al., 2016) in MT cells. Post-experimental histology confirmed that both indicators expressed well in the cytoplasm and membrane of MT cells (Figure 7A). In response to odorant stimulation, jRGECO1a signals were apparent both in an activated glomerulus as well as in the apical dendrites of the MT cells innervating it, while SF-iGluSnFR signals were not apparent in apical dendrites (Figure 7B).

To assess the degree to which diverse inhalation-linked glutamate signaling drives diversity in MT responses, we first compared response dynamics at low inhalation rates. Inhalation-linked transients were apparent in both signals at 1 Hz inhalation, although the degree of modulation by inhalation was much less apparent in the calcium signal (see Figure 7B, right), reflecting either the slower decay kinetics of jRGECO1a or MT cell spiking that outlasted the inhalation-linked glutamate transient. Despite these kinetic differences, there was a high correspondence in the inhalation-

linked dynamics of the two signals, with different glomeruli showing the same relative differences in the onset latency and time to peak of the SF-iGluSnFR.A184S and jRGECO1a ITA trace (Figure 7C, 7D). Inhalation-linked glutamate transients always preceded or coincided with calcium transients imaged from the same glomerulus.

Notably, we also observed high - although not perfect - correspondence between the occurrence of 'spontaneous' glutamate and calcium transients occurring in the absence of odorant stimulation. The traces in Figure 7E show spontaneously occurring transients that co-occur in both channels in the majority of cases, with a smaller number of events appearing only in one or the other. Small-amplitude glutamate transients in the absence of calcium transients were most commonly seen. Such observations are consistent with small bursts of glutamatergic input occasionally failing to drive MT cell spiking (Figure 7E, top trace, arrows) and, less frequently, the occurrence of MT spike bursts in the absence of coherent glutamatergic input (Figure 7E, bottom trace, arrow).

To compare the diversity of odorant-evoked response patterns seen in these two signals over a time-scale involving multiple inhalations, we performed dual-color imaging using the same 23 odorant panel as for the single-color imaging (in 5 fields of view from 3 mice) but using 3-sec rather than 2-sec presentations (Figure 8A). We saw the same range of response patterns in these experiments as in the single-color experiments, including sustained, rapidly adapting, facilitating and suppressive components (Figure 8A-C). Overall, there was a striking degree of correspondence in response patterns of the two signals, apparent both in single trials (Figure 8A) and in trial-averaged response maps and traces (Figure 8B, C). Rare cases of lack of correspondence between glutamate and calcium signals are shown for glomerulus 3 in Figure 8A, where 4 of the 10 odorants elicit suppression in the jRGECO1a signal; in three of these cases (arrows, Figure 8A), SF-iGluSnFR elicits a biphasic response consisting of a brief initial increase followed by a decrease in glutamate; the initial excitatory transient is not apparent in the calcium signal.

We quantified the correspondence between SF-iGluSnFR and jRGECO response patterns in several ways. First, we computed correlation coefficients between the two signals for each glomerulus-odor pair tested. In general, correlation coefficients were high: for all glomerulus-odor pairs showing a significant response in at least one of

the signals (using the conservative ± 7 SD above baseline criterion; n = 526 G-O Pairs, 3 mice), the mean correlation (Pearson's *r*) was 0.80 ± 0.18 (SD). We also examined the concordance between excitatory response types reflected in the two signals. There was strong concordance in glomeruli showing purely excitatory responses as measured with SF-iGluSnFR and jRGECO: 70% (244/350) of glomerulus-odor pairs with an excitatory SF-iGluSnFR signal also showed a significant jRGECO response, and 79% (244/309) of glomeruli with significant jRGECO increases showed excitatory SF-iGluSnFR signals.

Comparing concordance between pre- and postsynaptic signals among suppressive responses could reveal differential impacts of inhibitory inputs to MT cells - for example by feedforward or lateral inhibition. Such an analysis was difficult: while responses with suppressive components were clearly apparent even on single trials (i.e., Figure 8A), their small amplitude and the relatively few repeat trials given (3 - 4 per odorant) resulted in a likely underestimation of their prevalence based on the strict significance criteria we used. Nonetheless, jRGECO responses with suppressive components were detected significantly more frequently than SF-iGluSnFR responses, being present in 1.5% (55/3788) versus 0.4% (15/3788) of all glomerulus-odor pairs, and 15% versus 4% of all significant responses (Chi-Square statistic = 23.07, $p < 0.0001$). Notably, suppressive jRGECO responses were essentially never seen along with excitatory SF-iGluSnFR responses (detected in 1 of 55 cases, which is approaching the false positive rate). Thus, while preliminary, these results are consistent with a model in which interglomerular inhibition suppresses MT cell spiking in a small fraction of glomeruli (Whitesell et al., 2013; Economo et al., 2016; Liu et al., 2016), but are inconsistent with a model in which feedforward inhibition suppresses MT cell spiking in glomeruli receiving weak excitatory input (Gire and Schoppa, 2009; Cleland and Linster, 2012).

DISCUSSION

Temporally complex patterns of excitation and inhibition are a hallmark feature of odor-evoked activity among principal cells (MT cells) of the OB. Features of this complexity include odorant- and glomerulus-specific latency differences relative to

inhalation, suppressive response components, nonlinear concentration dependence, and decorrelation of glomerular odor representations over multiple samples (Spors et al., 2006; Patterson et al., 2013; Economo et al., 2016; Diaz-Quesada et al., 2018). Each of these features has been hypothesized to play an important role in coding olfactory information and most have been attributed to emergent properties of excitatory and inhibitory circuit interactions. Here, by directly imaging glutamate signaling onto MT cell dendrites of OB glomeruli, we observed a striking degree of complexity in this signaling that included heterogeneity both on the time-scale of a single inhalation or respiratory cycle and over a slower time scale involving repeated samples of odorant. Indeed, by simultaneously imaging both presynaptic glutamate and postsynaptic calcium from MT cells in the same glomerulus, we found a high correspondence in response patterns on time scales of a single inhalation and across multiple inhalations. Furthermore, diverse glutamatergic inputs to MT cells persisted after pharmacological blockade of postsynaptic activity, implicating direct inputs from OSNs as the primary source of this diversity. These results suggest a model of OB circuit function in which the dynamics of sensory input can account for much of the diversity of MT cell responses that are thought to mediate identity- and timing-based odor codes in vivo. Genetically encoded reporters of neurotransmitter signaling have emerged as useful tools for the dissection of neural circuits (Marvin et al., 2013; Patriarchi et al., 2018; Sun et al., 2018; Marvin et al., 2019), by allowing for monitoring of defined presynaptic inputs separately from (and simultaneously with) postsynaptic activation. This study demonstrates the utility of iGluSnFR and its second-generation 'SF'-variants to robustly report glutamate signaling onto MT cells with high signal-to-noise ratios, high temporal fidelity, and in both anesthetized and awake preparations. Even the lowest-affinity SF-variant, S72A, yielded easily detectable signals, albeit with greatly reduced sensitivity. Advantages for glutamate imaging in the OB relative to other brain areas such as cortex may be the high density of glutamatergic synapses in the glomerular neuropil, the high degree of convergence of OSNs activated near-simultaneously within a glomerulus, and the high probability for glutamate release from the OSN presynaptic terminal (Murphy et al., 2004). We were also able to image glutamate release from MT cell lateral dendrites using the higher-affinity variant A184S, indicating that SF-iGluSnFR may be useful for

mapping the transmission of odor information from MT cells to granule cells via their lateral dendrites.

Circuit mechanisms of diversity in glutamate signaling

OSN inputs converging on a glomerulus have long been known to respond with different latencies relative to inhalation in a glomerulus- and odor-specific manner (Spors et al., 2006; Carey et al., 2009; Short and Wachowiak, 2019); indeed we observed a close match in the range of response latencies for SF-iGluSnFR signals and those measured from OSN presynaptic terminals (e.g., Figure 2D). We also saw variation in other aspects of inhalation-linked glutamate dynamics - most notably response duration (e.g., Figure 2B, 2C), with the duration of the inhalation-linked glutamate transients ranging from as short as 200 msec to over 1.5 sec depending on the glomerulus-odor pair. Such differences likely have substantial impacts on the temporal dynamics of MT cell spiking and, potentially, on the activation of inhibitory OB circuits.

Glutamatergic signaling onto MT cells also showed complex dynamics over a slower time scale spanning multiple inhalations that could include adaptation, facilitation, or biphasic response patterns. Such complexity could arise entirely from presynaptic mechanisms, such as adaptation of OSNs or depression of OSN transmitter release (Murphy et al., 2004; Lecoq et al., 2009), or peripheral effects related to odorant sorption (Zhao et al., 2006; Yang et al., 2007). Regardless of mechanism, these results indicate that MT cell excitation is not a simple linear combination of responses to a single inhalation, as has been suggested by some earlier studies (Gupta et al., 2015). Comparable nonlinearities and richness in response kinetics have been well-characterized in Drosophila OSNs, where such features can be attributed to odorant receptor identity (Hallem and Carlson, 2006; Mathew et al., 2013).

A second potential source of diverse glutamate signaling onto MT cells is feedforward disynaptic excitation mediated by external tufted (ET) cells, which are thought to be a major source of glutamatergic drive throughout the glomerulus and a primary driver of MT cell excitation (Hayar et al., 2004; De Saint Jan et al., 2009; Gire et al., 2012; Gire et al., 2019). This disynaptic glutamatergic pathway allows for inhibitory

circuits to regulate MT cell excitability through their action on ET cells (Whitesell et al., 2013; Banerjee et al., 2015; Liu et al., 2016). A third potential source of diversity in MT cell glutamate signals is MT cells themselves, via dendritic release of glutamate from their apical tuft (Isaacson, 1999; Najac et al., 2015). The degree to which these different pathways drive MT cell excitation *in vivo* remains uncertain.

If ET cells or dendritic release from MT cells contribute substantial glutamatergic signals on MT cells, then pharmacological blockade of postsynaptic excitation with ionotropic glutamate receptor antagonists should have strongly reduced most odor-evoked glutamate signals in dorsal glomeruli. Instead, glutamate signals showed, overall, no significant change in mean or peak amplitude, and in fact showed an *increase* in the amplitude of glutamate signals over multiple inhalations of odorant. Distinct odorant- and glomerulus-specific temporal patterns of glutamate signals over the time-scale of several seconds remained largely unchanged (e.g., Figure 5C). These results indicate that the glutamate signals imaged from OB glomeruli do in fact represent glutamatergic input to, as opposed to glutamate release from, MT cells. While it possible that, in our experiments, either iGluSnFR or SF-iGluSnFR was expressed on ET cells as well as on superficial tufted cells, both of which are thought to receive largely monosynaptic OSN input (Gire et al., 2012) (Hayar et al., 2004), all preparations processed for post-hoc histology confirmed expression in substantial numbers of mitral cells (e.g., Figure 1A, Figure 7A). Thus, the lack of reduction in glutamate signal after blockade of postsynaptic activity suggests that OSN constitute a major source of glutamatergic input to mitral as well as tufted cells.

This result is surprising in light of numerous recent studies from OB slices suggesting that ET cells provide a large fraction - or even the majority of - glutamatergic input to MT cells via spillover from the ET - to - periglomerular cell synapse (Isaacson, 1999; De Saint Jan et al., 2009; Najac et al., 2011; Gire et al., 2012; Liu et al., 2016; Gire et al., 2019). At present we can only provide speculative explanations for these different results. For example, it is possible that glutamate spillover contributes less to MT cell drive *in vivo* than in OB slices, due to more effective transporter function at body temperature or in intact tissue. The dynamics of odorant-evoked OSN inputs, which involve asynchronous release from different OSN terminals in a glomerulus, may also

favor direct transmission from OSNs over indirect input from ET cells (Vaaga and Westbrook, 2016). Further investigation of the odorant-evoked activity patterns of ET cells in vivo, relative to that of OSN inputs to the same glomerulus, would be helpful in addressing these questions. As for the modest *increase* in glutamatergic input to MT cells with sustained odorant presentation that we observed after postsynaptic blockade, a reasonable explanation is that presynaptic inhibition of OSN terminals limits glutamate signaling over this time-frame (Wachowiak et al., 2005; Pírez and Wachowiak, 2008).

A remaining concern in interpreting MT cell glutamate signals and their correspondence with Ca^{2+} signals in the same cells is that glomerular Ca^{2+} signals could largely reflect subthreshold synaptic input, as opposed to MT cell action potential firing that back-propagates into the tuft, which would of course lead to overestimation of the correspondence between glutamatergic input and MT cell output patterns. However, previous studies suggest that back-propagating action potentials are the predominant driver of Ca^{2+} signals in the MT cell apical tuft (Charpak et al., 2001; Debarbieux et al., 2003), and we have observed a near-perfect correlation among odor-evoked Ca^{2+} signals in the apical tuft, shaft, and soma (Economo et al., 2016). Second, close inspection of dual-color imaging data revealed numerous cases of SF-iGluSnFR transients that fail to drive Ca^{2+} signals in the same glomerulus, especially when these transients were rapid or small in amplitude (e.g., Figure 7B, 7C; Figure 8A). Thus, while additional experiments focused on these issues will be helpful, our observations suggest that the high correspondence between SF-iGluSnFR and jRGECO signals seen in MT cells largely reflects the strong contribution of feedforward excitatory signaling to the dynamics of MT cell output patterns.

Impacts of glutamatergic dynamics on models of odor coding

Our data on the dynamics of glutamatergic input to MT cells provides new information that further inform models of how olfactory information is represented during natural odor sampling. The faster onset and decay times of SF-iGluSnFR relative to other genetically-encoded reporters such as GCaMPs allow us to better monitor neural dynamics in the frequency range of respiration or sniffing in behaving mice, which ranges from approximately 2 – 10 Hz (Wesson et al., 2008). This advantage was plainly

evident in our dual-color imaging experiments, in which jRGECO1a signals showed little modulation of their signal even at 2 Hz artificial inhalation, while SF-iGluSnFR signals imaged in the same trial were strongly modulated (e.g., Figure 7B). In fact, we were able to observe clear glutamate transients from each inhalation in awake, head-fixed mice at sniff frequencies up to and, in some cases, exceeding 5 Hz. This improved temporal fidelity will be important in addressing hypotheses about determinants of the relative timing of excitatory inputs to MT cells in different glomeruli and the role of this timing in odor coding.

Several important results emerged from our initial dataset of glutamate dynamics in awake mice. First, we found that the relative magnitudes of glutamate signal across different glomeruli changed over the course of an odor presentation, suggesting that odorant representations evolve in the first few seconds of repeated sampling of odorant. This result is consistent with recent studies that found dynamic odor representations on a similar time scale at the level of MT cell spiking (Patterson et al., 2013; Diaz-Quesada et al., 2018). Second, we found that a substantial fraction of odorant-evoked glutamate signals showed minimal or no respiratory patterning, consisting instead of tonic increases in glutamate when odorant was present. If a similar fraction of MT cells fail to show respiratory patterning in their spike timing in awake mice, this result has implications for theories of odor identity or intensity coding that are based on the timing of MT cell spikes within the breathing cycle (Chaput, 1986; Schaefer and Margrie, 2007; Wilson et al., 2017; Li et al., 2019). Third, in both awake and in anesthetized mice, we found that the temporal evolution of glutamate responses as well as the degree of inhalation-linked patterning appeared to vary systematically across different odorants and as a function of concentration. Further experiments are necessary to understanding the determinants of these glutamate dynamics - for example, whether they are determined by the affinity and intensity of an odorant relative to the dynamic range of a particular glomerulus-odorant pair, or instead by properties of odorant sorption in the olfactory epithelium.

Finally, the close correspondence between patterns of glutamatergic inputs to and correlates of spike output from MT cells, revealed by our dual-color imaging results, runs counter to predictions from several canonical models of how OB circuits transform

odor representations. In the spatial domain, we saw no evidence for broadly-organized inhibition surrounding glomeruli receiving excitatory inputs, as one might expect from models of center-surround or global inhibition (Luo and Katz, 2001; Banerjee et al., 2015) . We also saw no evidence for suppression of MT cell output in glomeruli receiving weak, or slow, excitatory inputs, as has been predicted from models of feedforward inhibition (Gire and Schoppa, 2009; Cleland and Linster, 2012). Thus, transformations of odor representations by OB circuitry- at least in the spatial and temporal domains - may be more limited than generally thought. This is not to say that inhibitory circuits are unimportant; instead their function may be to shape response features such as sensitivity and response gain by acting coincident with excitation. Such a model would be more similar to the function of many inhibitory circuits in cortex, which are reliant on and closely coupled to excitation (Isaacson and Scanziani, 2011). The growing toolbox of reporters of neurotransmitter signaling, combined with optical or electrophysiological readouts of postsynaptic activity in defined cell types, should enable a finer dissection of the interplay between excitation and inhibition as odor information is processed in the behaving animal.

MATERIALS AND METHODS

Animals

Experiments were performed on male and female transgenic mice expressing Cre recombinase (Cre) in defined neural populations with single or dual viral expression of the optical indicator of interest. Mouse strains used were: Pcd-Cre (Tg(Pcdh21-cre)BYoko), Gensat Stock #030952-UCD; OMP-Cre (Tg(Omp-tm4-Cre)Mom), JAX Stock #006668, and Tbet-Cre (Tg(Tbx21-cre)1Dlc) (Haddad et al., 2013), JAX Stock # 024507. Mice ranged from 3-8 months in age. Mice were housed up to 4/cage and kept on a 12/12 h light/dark cycle with food and water available ad libitum. All procedures were carried out following the National Institutes of Health Guide for the Care and Use of Laboratory Animals and were approved by the University of Utah Institutional Animal Care and Use Committee.

Viral vector expression

Viral vectors driving Cre-dependent expression of iGluSnFR and jRGECO1a (Marvin et al., 2013; Dana et al., 2016; Marvin et al., 2018) were obtained from the University of Pennsylvania Vector Core (AAV1 or 5 serotype, AAV.hSynap-FLEX.iGluSnFR). SF-iGluSnFR variants were obtained from either HHMI Janelia Campus (AAV1 or 5 serotype, pAAV.hSynap-FLEX.SF-iGluSnFR.A184V, pAAV.hSynap-FLEX.SF-iGluSnFR.A184S) or Addgene Vector Cores (AAV1 serotype, pAAV.hSynap-FLEX.SF-iGluSnFR.S72A, #106182). Each vector was targeted into either the mitral cell layer (MCL) or the deep external plexiform layer (EPL) of the OB using pressure injections in glass pipettes, as described previously (Wachowiak et al., 2013; Short and Wachowiak, 2019). For coinjection of jRGECO1a and SF-iGluSnFR.A184S, each virus was diluted 1:10 and injected in separate pipettes through the same craniotomy. After injection, mice were given carprofen (Rimadyl, S.C., 5 mg/kg; Pfizer) as an analgesic and enrofloxacin (Baytril, I.M., 3 mg/kg; Bayer) as an antibiotic immediately before and 24 hours after surgery. Mice were singly housed after surgery on ventilated racks and used 21-35 days after virus injection. In some mice, viral expression was characterized with post-hoc histology using native fluorescence.

In vivo two photon imaging

Two-photon imaging in anesthetized mice was performed as described previously (Wachowiak et al., 2013; Economo et al., 2016). Mice were initially anesthetized with pentobarbital (50 - 90 mg/kg) then maintained under isoflurane (0.5 – 1% in O_2) for data collection. Body temperature and heart rate were maintained at 37 ºC and ~ 400 beats per minute. Mice were double tracheotomized and isoflurane was delivered passively via the tracheotomy tube without contaminating the nasal cavity (Eiting and Wachowiak, 2018). Two-photon imaging occurred after removal of the bone overlying the dorsal olfactory bulb and stabilizing the brain surface with agarose and a glass coverslip.

Imaging was carried out with a two-photon microscope (Sutter Instruments or Neurolabware) coupled to a pulsed Ti:Sapphire laser (Mai Tai HP, Spectra-Physics; or Chameleon Ultra, Coherent) at 920-940 nm and controlled by either Scanimage (Pologruto et al., 2003) or Scanbox software. Imaging was performed through a 16X, 0.8 N.A. objective (Nikon) and emitted light detected with GaAsP photomultiplier tubes (Hamamatsu). Fluorescence images were acquired using unidirectional resonance scanning at 15.2 or 15.5 Hz. For SF-iGluSnFR.S72A imaging, bidirectional scanning at 30Hz was utilized to capture faster responses. For dual-color imaging, a second laser (Fidelity-2; Coherent) was utilized to optimally excite jRGECO1a and emitted red fluorescence collected with a second PMT, as described previously (Short and Wachowiak, 2019).

In vivo pharmacology

In vivo pharmacology was carried out after removing the bone and dura overlying the dorsal olfactory bulb, using protocols described previously (Pírez and Wachowiak, 2008; Brunert et al., 2016). Drug solutions (1 mM NBQX / 2 mM APV) were dissolved in Ringers solution and applied in bulk to the dorsal OB without the use of agarose or coverslip. We waited at least 10 minutes after drug application to allow for absorption into the tissue and temperature equilibration.

Odorant stimulation

In some experiments, odorants were presented as precise dilutions from saturated vapor (s.v.) in cleaned, desiccated air using a custom olfactometer under computer control, as described previously (Bozza et al., 2004; Economo et al., 2016). Odorants were presented for durations ranging from 2 - 8 sec. Clean air was passed across the nostrils in between trials to avoid contribution from extraneous odorants in the environment. Odorants were pre-diluted in solvent (1:10 or 1:25 in mineral oil or medium chain triglyceride oil) to allow for lower final concentrations and then diluted to concentrations ranging from .3% to 3% s.v. Relative increases in concentration were confirmed with a photoionization detector (miniRAE Lite, PGM-7300, RAE Systems) 3 cm away from the flow dilution port. Estimated final concentrations of odorants used ranged from 0.01 – 300 ppm, depending on vapor pressure and s.v. dilution (Table 1). For experiments testing a larger panel of odorants (e.g., Figures 3 and 5, see Table 1), we used a novel, recently described olfactometer design that allowed for rapid switching between odorants with minimal cross-contamination (Burton et al., 2019). Here, odorants were presented for 2 or 3 seconds, in random order from among a bank of 12 odorant cartridges, using 10 second interstimulus intervals. Odorant preparation and presentation was as described in (Burton et al., 2019), using an eductor nozzle for optimal mixing in a carrier stream of filtered air. The end of the eductor was placed 5-7 cm away from the nose. With the configuration used, estimated dilutions of odorant were approximately 1.5% s.v.; odorants were prediluted to achieve relatively sparse activation of dorsal glomeruli (Burton et al., 2019). Estimated final concentrations ranged from 0.01 – 16 ppm (Table 1).

Awake Imaging

Imaging in awake, head-fixed mice was performed through a chronic imaging window implanted over the dorsal OB, using protocol adapted from (Holtmaat et al., 2009; Goldey et al., 2014; Chu et al., 2016). The imaging window consisted of a custom double coverslip with minimum diameter of 1.5 mm. SF-iGluSnFR virus (500-750 nL of pAAV.hSynap.SF-iGluSnFR.A184V.WPRE) was injected at a depth of 250 µm at the time of window implant. Animals were allowed to recover for a minimum of two days post-surgery and then acclimated to the imaging rig for one 30-minute session the day

prior to imaging. Imaging sessions lasted from 30-60 minutes per day, over the course of several days. The behavior and imaging apparatus has been described previously (Economo et al., 2016). Mice were naïve to the odors at their first imaging session. Respiration (sniff) signals were obtained with an external flow sensor (FBAM200DU, First Sensor, AG, Berlin) in front of the animal's right nostril (Jordan et al., 2018).

Data Analysis

Image analysis was performed using custom software written in MATLAB (Mathworks). For figure display, odorant response maps were displayed using ΔF values rather than ΔF/F to minimize noise from nonfluorescent regions. Activity maps were scaled as indicated in the figure and were kept to their original resolution (512 x 512 pixels) and smoothed using a Gaussian kernel with σ of 1 pixel. For time-series analysis, regions of interest (ROIs) were chosen manually based on the mean fluorescence image and were further refined based on odorant response ΔF maps, then all pixels averaged within an ROI. All signals were upsampled to 150 Hz for analysis using the MATLAB pchip function. Time-series were typically computed and displayed as ΔF/F, with F defined as the mean fluorescence in the 1-2 sec prior to odorant onset.

For analysis of inhalation-linked dynamics, inhalation-triggered average (ITA) responses were generated by averaging each inhalation (delivered at 0.25 Hz) over a 70 sec odorant presentation (17 inhalations averaged in total). Onset latencies, peak responses, and ITA durations (full-width at half-maximum) were defined as previously (Short and Wachowiak, 2019). To calculate decay time-constants (Figure 1), a single exponential was fitted from the peak of the unfiltered ITA trace and extending to the end of the trace. Time-to-peak values were calculated from unfiltered ITAs as the time from the inhalation start to the peak of the response.

For analysis of odorant-evoked dynamics over multiple sniffs, responses to 3 - 8 presentations of odorant were averaged before analysis. Changes in response amplitude over time, or T_2-T_1/T_{max} (Figure 4) were calculated as the difference in amplitude between the peak ΔF following the first (T_1) and the second-to-last (T_2) inhalation during odorant presentation, divided by the maximum ΔF during the 4 sec

odor presentation. Modulation of the iGluSnFR signal by inhalation was measured as coherence to a 2Hz sine wave, using the mscohere function in MATLAB.

To analyze response patterns across the 23-odorant panel (i.e., Figures 3, 5 and 8) , responses were averaged across 3 - 4 randomized presentations of each odorant. Responses were classified as having significant excitatory and/or suppressive components as follows: First, each averaged response for an ROI-odor pair was low-pass Gaussian filtered at 2 Hz (to test for excitatory responses) or 0.5 Hz (for suppressive responses) and z-scored using a baseline from 0.5 to 2 sec prior to odorant onset, with z defined as the SD of the baseline period concatenated for all 23 odorant responses for each ROI. Peak excitation was measured as 95% of the maximum signal during the 3- or 4-sec odorant presentation; suppressive responses were measured as the 15th percentile of all values in a time-window from odorant onset to 500 msec after odorant offset. We then used a very conservative criterion for significance of z = $\pm$7 SD for identifying significant excitatory or suppressive response components. This cutoff was chosen to yield a false positive rate of approximately 1% (based on visual inspection of a subset of traces).

Glomerular tuning was characterized from response matrices thresholded according to these significance values, using a measure of lifetime sparseness (Schlief and Wilson, 2007):

$$S = \{1 - [(\sum N_{j=1} r_j / N)^2 / \sum N_{j=1} (r_j^2 / N)\} / [1 - (1/N)]$$

Where N is number of odors and r_j is the thresholded z-scored value for a given glomerulus of the response to odor j. Sparseness was calculated separately for excitatory and suppressive response components.

Time-dependent decorrelation of odorant response patterns across glomeruli (Figures 3 and 6) was calculated from z-scored time series as described above, taken from all glomeruli in a field of view without thresholding. Each odorant response was binned into five time bins (each of 387 msec) spanning the length of odorant presentation but omitting the first 65 msec to account for delays in odorant onset. Pearson's correlation coefficient (*r*) was calculated using the response amplitudes across all ROIs in the first time bin as a vector, compared to the same vector taken from each subsequent bin. We calculated an overall correlation time series by computing the

mean and s.e.m. for all 111 significant odorant responses, pooled across all fields of view.

To correlate iGluSnFR and jRGECO1a signals in the dual-color imaging experiments, Pearson's correlation coefficients (*r*) were calculated from each average odor response after low-pass filtering at 2 Hz, over a time-window from 2 sec before to 10 sec after odor onset.

For analysis of inhalation-linked timing of glutamate signals in awake mice, we restricted analysis to inhalations occurring at a minimum period of 200 msec (5 Hz respiration rate). Inhalation timing was detected from the external flow sensor using peak/trough detection and maximal slopes of the flow signal. Inhalation peak was defined as the trough of the external flow signal; inhalation onset was defined as the maximal slope of the transition from exhalation to inhalation. In a subset of trials we found a consistent delay of 60 msec between time of inhalation start and time of inhalation peak; because inhalation peak timing was a more robust measure, we generated inhalation-triggered average iGluSnFR signals based on inhalation peak, then adjusted latency and time-to-peak measurements by 60 msec, to express results relative to inhalation onset. ITAs were generated by averaging the unfiltered optical signal taken from 1 sec before to 3 sec after the peak of inhalation.

Statistical tests were performed either in Origin (OriginLab Corp.), MATLAB (Mathworks) or R (version 3.3.2). Parametric tests were used only on datasets determined to be normally distributed. Summary statistics are reported as mean ± standard deviation (SD), unless otherwise stated.

ACKNOWLEDGEMENTS

We thank L. Looger and J. Marvin and the GENIE project from HHMI Janelia Research Campus for sharing SF-iGluSnFR virus. We also thank M. Economo, D. Brunert and Y. Tsuno for initial characterization of iGluSnFRs, G. Vasquez-Opazo, R. Kummer and J. Ball for technical assistance, and T. Rust for data analysis software. S. Burton, S. Short, I. Youngstrom, provided helpful feedback and discussion. This work was supported by the NINDS T32NS076067 (to A.K.M) and NIDCD R01DC006441 (to M.W.), R01DC006441-13S1 (to A.K.M), and F32DC015389 (to T.P.E).

COMPETING INTERESTS

These authors declare no competing financial interests.

CONTRIBUTIONS

A.K.M and M.W. designed research. A.K.M, T.P.E, and M.W. performed research, A.K.M., T.P.E., and M.W. analyzed data, A.K.M. and M.W. wrote the paper.

REFERENCES

Banerjee A, Marbach F, Anselmi F, Koh MS, Davis MB, Garcia da Silva P, Delevich K, Oyibo HK, Gupta P, Li B, Albeanu DF (2015) An Interglomerular Circuit Gates Glomerular Output and Implements Gain Control in the Mouse Olfactory Bulb. Neuron 87:193-207.

Bischofberger J, Jonas P (1997) Action potential propagation into the presynaptic dendrites of rat mitral cells. J Physiol 504 (Pt 2):359-365.

Bozza T, McGann JP, Mombaerts P, Wachowiak M (2004) In vivo imaging of neuronal activity by targeted expression of a genetically encoded probe in the mouse. Neuron 42:9-21.

Brunert D, Tsuno Y, Rothermel M, Shipley MT, Wachowiak M (2016) Cell-Type-Specific Modulation of Sensory Responses in Olfactory Bulb Circuits by Serotonergic Projections from the Raphe Nuclei. J Neurosci 36:6820-6835.

Burton SD (2017) Inhibitory circuits of the mammalian main olfactory bulb. J Neurophysiol 118:2034-2051.

Burton SD, Wipfel M, Guo M, Eiting TP, Wachowiak M (2019) A Novel Olfactometer for Efficient and Flexible Odorant Delivery. Chem Senses 44:173-188.

Carey RM, Verhagen JV, Wesson DW, Pirez N, Wachowiak M (2009) Temporal Structure of Receptor Neuron Input to the Olfactory Bulb Imaged in Behaving Rats. J Neurophysiol 101:1073-1088.

Chaput MA (1986) Respiratory-phase-related coding of olfactory information in the olfactory bulb of awake freely-breathing rabbits. Physiol Behav 36:319-324.

Charpak S, Mertz J, Beaurepaire E, Moreaux L, Delaney K (2001) Odor-evoked calcium signals in dendrites of rat mitral cells. Proc Natl Acad Sci U S A 98:1230-1234.

Chen WR, Midtgaard J, Shepherd GM (1997) Forward and backward propagation of dendritic impulses and their synaptic control in mitral cells. Science 278:463-467.

Chu MW, Li WL, Komiyama T (2016) Balancing the Robustness and Efficiency of Odor Representations during Learning. Neuron 92:174-186.

Cleland TA, Linster C (2012) On-Center/Inhibitory-Surround Decorrelation via Intraglomerular Inhibition in the Olfactory Bulb Glomerular Layer. Front Integr Neurosci 6:5.

Dana H, Mohar B, Sun Y, Narayan S, Gordus A, Hasseman JP, Tsegaye G, Holt GT, Hu A, Walpita D, Patel R, Macklin JJ, Bargmann CI, Ahrens MB, Schreiter ER, Jayaraman V, Looger LL, Svoboda K, Kim DS (2016) Sensitive red protein calcium indicators for imaging neural activity. eLife 5:e12727.

De Saint Jan D, Hirnet D, Westbrook GL, Charpak S (2009) External Tufted Cells Drive the Output of Olfactory Bulb Glomeruli. J Neurosci 29:2043-2052.

Debarbieux F, Audinat E, Charpak S (2003) Action potential propagation in dendrites of rat mitral cells in vivo. J Neurosci 23:5553-5560.

Diaz-Quesada M, Youngstrom IA, Tsuno Y, Hansen KR, Economo MN, Wachowiak M (2018) Inhalation Frequency Controls Reformatting of Mitral/Tufted Cell Odor Representations in the Olfactory Bulb. J Neurosci 38:2189-2206.

Economo MN, Hansen KR, Wachowiak M (2016) Control of Mitral/Tufted Cell Output by Selective Inhibition among Olfactory Bulb Glomeruli. Neuron.

Eiting TP, Wachowiak M (2018) Artificial Inhalation Protocol in Adult Mice. Bio Protoc 8.

Geramita M, Urban NN (2017) Differences in Glomerular-Layer-Mediated Feedforward Inhibition onto Mitral and Tufted Cells Lead to Distinct Modes of Intensity Coding. J Neurosci 37:1428-1438.

Gire DH, Schoppa NE (2009) Control of on/off glomerular signaling by a local GABAergic microcircuit in the olfactory bulb. J Neurosci 29:13454-13464.

Gire DH, Zak JD, Bourne JN, Goodson NB, Schoppa NE (2019) Balancing Extrasynaptic Excitation and Synaptic Inhibition within Olfactory Bulb Glomeruli. eNeuro 6.

Gire DH, Franks KM, Zak JD, Tanaka KF, Whitesell JD, Mulligan AA, Hen R, Schoppa NE (2012) Mitral Cells in the Olfactory Bulb Are Mainly Excited through a Multistep Signaling Path. The Journal of Neuroscience 32:2964-2975.

Goldey GJ, Roumis DK, Glickfeld LL, Kerlin AM, Reid RC, Bonin V, Schafer DP, Andermann ML (2014) Removable cranial windows for long-term imaging in awake mice. Nat Protoc 9:2515-2538.

Gupta P, Albeanu DF, Bhalla US (2015) Olfactory bulb coding of odors, mixtures and sniffs is a linear sum of odor time profiles. Nat Neurosci advance online publication.

Gurden H, Uchida N, Mainen ZF (2006) Sensory-evoked intrinsic optical signals in the olfactory bulb are coupled to glutamate release and uptake. Neuron 52:335-345.

Haddad R, Lanjuin A, Madisen L, Zeng H, Murthy VN, Uchida N (2013) Olfactory cortical neurons read out a relative time code in the olfactory bulb. Nat Neurosci 16:949-957.

Hallem EA, Carlson JR (2006) Coding of odors by a receptor repertoire. Cell 125:143-160.

Hayar A, Karnup S, Ennis M, Shipley MT (2004) External tufted cells: A major excitatory element that coordinates glomerular activity. J Neurosci 24:6676-6685.

Holtmaat A, Bonhoeffer T, Chow DK, Chuckowree J, De Paola V, Hofer SB, Hubener M, Keck T, Knott G, Lee WC, Mostany R, Mrsic-Flogel TD, Nedivi E, Portera-Cailliau C, Svoboda K, Trachtenberg JT, Wilbrecht L (2009) Long-term, high-resolution imaging in the mouse neocortex through a chronic cranial window. Nat Protoc 4:1128-1144.

Isaacson JS (1999) Glutamate spillover mediates excitatory transmission in the rat olfactory bulb. Neuron 23:377-384.

Isaacson JS, Strowbridge BW (1998) Olfactory reciprocal synapses: dendritic signaling in the CNS. Neuron 20:749-761.

Isaacson JS, Scanziani M (2011) How inhibition shapes cortical activity. Neuron 72:231-243.

Jordan R, Fukunaga I, Kollo M, Schaefer AT (2018) Active Sampling State Dynamically Enhances Olfactory Bulb Odor Representation. Neuron 98:1214-1228 e1215.

Junek S, Kludt E, Wolf F, Schild D (2010) Olfactory Coding with Patterns of Response Latencies. Neuron 67:872-884.

Lecoq J, Tiret P, Charpak S (2009) Peripheral adaptation codes for high odor concentration in glomeruli. J Neurosci 29:3067-3072.

Li A, Rao X, Zhou Y, Restrepo D (2019) Complex neural representation of odour information in the olfactory bulb. Acta physiologica:e13333.

Liu S, Puche AC, Shipley MT (2016) The Interglomerular Circuit Potently Inhibits Olfactory Bulb Output Neurons by Both Direct and Indirect Pathways. J Neurosci 36:9604-9617.

Luo M, Katz LC (2001) Response correlation maps of neurons in the mammalian olfactory bulb. Neuron 32:1165-1179.

Marvin JS, Shimoda Y, Magloire V, Leite M, Kawashima T, Jensen TP, Kolb I, Knott EL, Novak O, Podgorski K, Leidenheimer NJ, Rusakov DA, Ahrens MB, Kullmann DM, Looger LL (2019) A genetically encoded fluorescent sensor for in vivo imaging of GABA. Nat Methods 16:763-770.

Marvin JS, Borghuis BG, Tian L, Cichon J, Harnett MT, Akerboom J, Gordus A, Renninger SL, Chen T-W, Bargmann CI, Orger MB, Schreiter ER, Demb JB, Gan W-B, Hires SA, Looger LL (2013) An optimized fluorescent probe for visualizing glutamate neurotransmission. Nat Meth 10:162-170.

Marvin JS et al. (2018) Stability, affinity, and chromatic variants of the glutamate sensor iGluSnFR. Nat Methods 15:936-939.

Mathew D, Martelli C, Kelley-Swift E, Brusalis C, Gershow M, Samuel AD, Emonet T, Carlson JR (2013) Functional diversity among sensory receptors in a Drosophila olfactory circuit. Proc Natl Acad Sci U S A 110:E2134-2143.

Matsumoto H, Kashiwadani H, Nagao H, Aiba A, Mori K (2009) Odor-Induced Persistent Discharge of Mitral Cells in the Mouse Olfactory Bulb. J Neurophysiol 101:1890-1900.

Matsuno T, Kiyokage E, Toida K (2017) Synaptic distribution of individually labeled mitral cells in the external plexiform layer of the mouse olfactory bulb. J Comp Neurol 525:2611.

McGann JP, Pírez N, Gainey MA, Muratore C, Elias AS, Wachowiak M (2005) Odorant representations are modulated by intra- but not interglomerular presynaptic inhibition of olfactory sensory neurons. Neuron 48:1039-1053.

Murphy GJ, Glickfeld LL, Balsen Z, Isaacson JS (2004) Sensory neuron signaling to the brain: properties of transmitter release from olfactory nerve terminals. J Neurosci 24:3023-3030.

Najac M, De Saint Jan D, Reguero L, Grandes P, Charpak S (2011) Monosynaptic and Polysynaptic Feed-Forward Inputs to Mitral Cells from Olfactory Sensory Neurons. The Journal of Neuroscience 31:8722-8729.

Najac M, Sanz Diez A, Kumar A, Benito N, Charpak S, De Saint Jan D (2015) Intraglomerular lateral inhibition promotes spike timing variability in principal neurons of the olfactory bulb. J Neurosci 35:4319-4331.

Padmanabhan K, Urban NN (2010) Intrinsic biophysical diversity decorrelates neuronal firing while increasing information content. Nat Neurosci 13:1276-1282.

Patriarchi T, Cho JR, Merten K, Howe MW, Marley A, Xiong WH, Folk RW, Broussard GJ, Liang R, Jang MJ, Zhong H, Dombeck D, von Zastrow M, Nimmerjahn A, Gradinaru V, Williams JT, Tian L (2018) Ultrafast neuronal imaging of dopamine dynamics with designed genetically encoded sensors. Science 360.

Patterson MA, Lagier S, Carleton A (2013) Odor representations in the olfactory bulb evolve after the first breath and persist as an odor afterimage. Proc Natl Acad Sci U S A 110:E3340-3349.

Pírez N, Wachowiak M (2008) In vivo modulation of sensory input to the olfactory bulb by tonic and activity-dependent presynaptic inhibition of receptor neurons. J Neurosci 28:6360-6371.

Ressler KJ, Sullivan SL, Buck LB (1994) Information coding in the olfactory system: evidence for a stereotyped and highly organized map in the olfactory bulb. Cell 79:1245-1255.

Richter FG, Fendl S, Haag J, Drews MS, Borst A (2018) Glutamate Signaling in the Fly Visual System. iScience 7:85-95.

Schaefer AT, Margrie TW (2007) Spatiotemporal representations in the olfactory system. Trends Neurosci 30:92-100.

Schlief ML, Wilson RI (2007) Olfactory processing and behavior downstream from highly selective receptor neurons. Nat Neurosci.

Schoppa NE, Urban NN (2003) Dendritic processing within olfactory bulb circuits. Trends Neurosci 26:501-506.

Shao Z, Puche AC, Liu S, Shipley MT (2012) Intraglomerular inhibition Shapes the Strength and Temporal Structure of Glomerular Output. J Neurophysiol.

Short SM, Wachowiak M (2019) Temporal Dynamics of Inhalation-Linked Activity across Defined Subpopulations of Mouse Olfactory Bulb Neurons Imaged In Vivo. eNeuro 6:ENEURO.0189-0119.2019.

Shusterman R, Smear MC, Koulakov AA, Rinberg D (2011) Precise olfactory responses tile the sniff cycle. Nat Neurosci 14:1039-1044.

Spors H, Wachowiak M, Cohen LB, Friedrich RW (2006) Temporal dynamics and latency patterns of receptor neuron input to the olfactory bulb. J Neurosci 26:1247-1259.

Sun F et al. (2018) A Genetically Encoded Fluorescent Sensor Enables Rapid and Specific Detection of Dopamine in Flies, Fish, and Mice. Cell 174:481-496 e419.

Vaaga CE, Westbrook GL (2016) Parallel processing of afferent olfactory sensory information. J Physiol 594:6715-6732.

Vassar R, Chao SK, Sitcheran R, Nunez JM, Vosshall LB, Axel R (1994) Topographic organization of sensory projections to the olfactory bulb. Cell 79:981-991.

Verhagen JV, Wesson DW, Netoff TI, White JA, Wachowiak M (2007) Sniffing controls an adaptive filter of sensory input to the olfactory bulb. Nat Neurosci 10:631-639.

Wachowiak M, Shipley MT (2006) Coding and synaptic processing of sensory information in the glomerular layer of the olfactory bulb. Semin Cell Dev Biol 17:411-423.

Wachowiak M, McGann JP, Heyward PM, Shao Z, Puche AC, Shipley MT (2005) Inhibition of olfactory receptor neuron input to olfactory bulb glomeruli mediated by suppression of presynaptic calcium influx. J Neurophysiol 94:2700-2712.

Wachowiak M, Economo MN, Díaz-Quesada M, Brunert D, Wesson DW, White JA, Rothermel M (2013) Optical Dissection of Odor Information Processing In Vivo

Using GCaMPs Expressed in Specified Cell Types of the Olfactory Bulb. The Journal of Neuroscience 33:5285-5300.

Wesson DW, Donahou TN, Johnson MO, Wachowiak M (2008) Sniffing behavior of mice during performance in odor-guided tasks. Chemical Senses 33:581-596.

Whitesell JD, Sorensen KA, Jarvie BC, Hentges ST, Schoppa NE (2013) Interglomerular lateral inhibition targeted on external tufted cells in the olfactory bulb. J Neurosci 33:1552-1563.

Wilson CD, Serrano GO, Koulakov AA, Rinberg D (2017) A primacy code for odor identity. Nat Commun 8:1477.

Yang GC, Scherer PW, Zhao K, Mozell MM (2007) Numerical Modeling of Odorant Uptake in the Rat Nasal Cavity. Chem Senses 32:273-284.

Yokoi M, Mori K, Nakanishi S (1995) Refinement of odor molecule tuning by dendrodendritic synaptic inhibition in the olfactory bulb. Proc Natl Acad Sci U S A 92:3371-3375.

Zhao K, Dalton P, Yang GC, Scherer PW (2006) Numerical modeling of turbulent and laminar airflow and odorant transport during sniffing in the human and rat nose. Chem Senses 31:107-118.

FIGURE LEGENDS

Figure 1. Characterization of iGluSnFRs as reporters of glutamatergic signaling onto MT cells.

A. Expression of iGluSnFR and SF-iGluSnFR in MT cells of the OB. Top: Confocal image stack showing expression in MT cells after AAV2.1.hSynap.Flex.SF-iGluSnFR.A184V in the OB of a Tbet-Cre mouse. White arrows indicate a tufted cell with expression in the soma and primary dendrite extending to the glomerular layer (GL). Bottom: Confocal image from the external plexiform layer (EPL) of a Pcdh21-Cre mouse injected with AAV2.5.hSynap.Flex.iGluSnFR, showing membrane surface expression in primary and lateral dendrites. MCL, mitral cell layer.

B. Top left: Mean fluorescence image taken in vivo, showing iGluSnFR expression in OB glomeruli from a Pcd-Cre mouse. Top right: ΔF image showing responses to ethyl butyrate (mean of 8 presentations, 2Hz inhalation). Bottom: Traces showing odorant-evoked iGluSnFR signal in three glomeruli, with dashed region expanded at right. Note distinct temporal responses across successive inhalations for each glomerulus.

C. Comparison of SF-iGluSnFR variants. Top: Traces showing unscaled ΔF/F (left) and peak-normalized (right) ITAs for the three SF-variants (see Text). Bottom: Cumulative fraction of peak ITA response magnitudes (left) and decay rates (right) across the population of significantly-responding glomerulus-odor pairs for each SF-variant.

D. Subcellular localization of SF-iGluSnFR signals. Top and bottom show two examples of SF-iGluSnFR.A184S responses imaged at high zoom from different glomeruli. Images show mean F (left) and ΔF response maps (right) to ethyl butyrate, showing localization of iGluSnFR signal to the glomerular neuropil (glom.), with a lack of signal on primary dendrites (pr. dend.) or MT cell somata (somas).

E. Traces showing responses to ethyl butyrate taken from the glomerular neuropil, primary dendrite, and MT somata (locations indicated in (D)), indicating negligible signal on the apical dendrite or somata.

F. Odorant-specific glutamate signals on MT cell lateral dendrites imaged with SF-iGluSnFR.A184S. Left: ΔF response maps evoked by two odorants, imaged from the same field of view in the superficial EPL. Each odorant elicits SF-iGluSnFR signal in

distinct combinations of lateral dendrites. Right: Traces showing evoked signals from the regions indicated at left, including excitatory and putative suppressive responses in different lateral dendrites.

Figure 2. Glomerular glutamate signals show diverse inhalation-driven dynamics.

A. Left: Mean fluorescence image of SF-iGluSnFR.A184V expression imaged in vivo. Right: Inhalation-triggered ΔF response maps for three odorants.

B. ITA response traces for the glomeruli indicated in (A). Traces are unfiltered averages across 17 inhalations. Left: ITAs from one glomerulus (ROI 5) responsive to 3 odorants, illustrating odorant-specific ITA dynamics. Right: ITAs from different glomeruli responsive to each of the three odorants, illustrating glomerulus-specific dynamics.

C. Plot of ITA onset latency, peak latency, and duration (FWHM, full-width half-max) for all responsive glomerulus-odor pairs using SF-iGluSnFR.A184S. Notch box plots (left) of latency values (right). Notch: median, square: mean, box edges: 25th and 75th percentile.

D. Cumulative fraction of median-subtracted, ITA onset latencies for SF-iGluSnFR.A184S signals, compared to those measured from GCaMP6f expressed in OSN axon terminals (see Text). Note similar range of onset latencies.

Figure 3. Glomerular glutamate signals show diverse temporal patterns across repeated samples of odorant.

A. Mean fluorescence (left) and ΔF response maps for 5 odorants imaged with SF-iGluSnFR.A184S (right). Odor numbers on the left side of the odorant map indicate odorant identification code for listed odor name (for reference to (B)). Colored text indicates odorants whose responses are shown in panels B, C and F.

B. Time-series of SF-iGluSnFR.A184S signal from 4 glomeruli, showing continuous signal during 3 repetitions of 12 odorants, presented in random order. Shaded rectangle indicates time of odorant presentations (2 sec duration). Signal is low-pass filtered at 0.5 Hz for display.

C. Average time-course of odorant-evoked responses in different glomeruli responsive to 4 of the 12 odorants from (B). Insets show change in response pattern across the

field of view from (A) over the duration of odorant presentation, expressed as Pearson's *r* relative to the initial response in successive time bins of 387 msec (see Text). Dotted line indicates r = 0.

D. 'Waterfall' plot showing time-course of odorant-evoked SF-iGluSnFR.A184S signal in all significantly-responding glomerulus-odor pairs (one pair per row), normalized to the peak ΔF/F for each pair. Suppressive responses are low-pass filtered at 0.5 Hz and excitatory responses are low pass filtered at 2 Hz.

E. Proportion of excitatory (Exc.), suppressive (Sup) and biphasic (Exc. & Sup.) responses across the responsive population (right), as well as the entire population of glomeruli (left).

F. Change in glutamate response patterns during odorant presentation, summarized over all presentations. Black plot shows mean correlation over time, averaged across all odorant presentations. Shaded area indicates s.e.m. Dot plot at right shows correlation coefficients at the final time bin for all presentations.

Figure 4. Odorant concentration has systematic impacts on glutamate signaling onto MT cells.

A. 'Waterfall' plots (left) and traces (right) showing time-course from select glomeruli showing original iGluSnFR signals in response to 3 concentrations of odorant for three different odorants (1x, 3x, 10x indicates relative concentration values; see Text). All data are from the same experiment and field of view. Only glomeruli showing significant responses at all 3 concentrations are shown. Inhalation frequency, 2 Hz; odorant duration, 4 seconds. Signals are unfiltered. Glomerular identity is color-coded with lines pointing to the traces. White dotted line indicates odor onset.

B. Change in iGluSnFR response amplitude from beginning to end of odorant presentation (T_2-T_1/T_{max}; inset illustrates definition of the measure, see Text), summarized for all analyzed glomerulus-odorant pairs (n = 189 glomerulus-odorant pairs from 4 mice). Note high variability and slight trend towards adaptation. Notch: median, square: mean, box edges: 25th and 75th percentiles.

C. Coherence of iGluSnFR signal to the 2 Hz inhalation frequency (see Text), measured for the same glomerulus-odorant pairs in (B), showing high variability across glomeruli and lower coherence at higher concentration.

D. Coherence values as a function of concentration, plotted separately for each of five odorants. Dot: median, error bars: quartiles. Note the persistently high coherence as concentration increases for 2-hexanone.

Figure 5. Persistence of diverse glutamate signaling onto MT cells after postsynaptic blockade.

A. Mean SF-iGluSnFR.A184S fluorescence (left) and ∆F response maps (right) f showing responses to two odorants before (Pre-drug) and after application of ionotropic receptor blockers (APV/NBQX).

B. SF-iGluSnFR.A184S signals from two glomeruli showing diverse temporal response patterns to different odorants. Left: Traces showing pre-drug average responses (mean of 4 presentations); Right: Traces showing responses after APV/NBQX application to the dorsal OB. Response to cyclohexylamine (bottom) shows a loss of the initial transient and replacement by tonic signal. Response to vinyl butyrate (top) shows increase in initial response magnitude and apparent loss of adaptation. Temporally distinct patterns of response patterns to other odorants persist after drug application.

C. Waterfall plots showing time-course of all responsive glomerulus-odor pairs in one experiment, before and after application of APV/NBQX. Each row is scaled to its own maximum in the pre-drug condition; row order is sorted by latency to peak in pre-drug condition.

D. Left: Mean and peak normalized response amplitudes after application of APV/NBQX, with distributions indicated as previously. Right: Scatter plot of T_2-T_1/T_{max} values before and after APV/NBQX application for all responsive glomerulus-odor pairs across 3 mice (each mouse indicated by color), showing decrease in adaptation for many pairs after application of APV/NBQX.

Figure 6. Diversity of glutamate dynamics imaged from MT cells in the awake mouse.

A. Top: mean SF-iGluSnFR.A184V fluorescence and Bottom: ∆F response map (ethyl butyrate) from the dorsal OB of an awake, head-fixed mouse. Right: Glutamate signals from 3 glomeruli (shown in (A)) during a single presentation of odorant (ethyl butyrate). Top trace shows respiration/sniffing as measured with an external flow sensor, with inhalation oriented downward. Lower left, snippet of signals from each glomerulus, illustrating temporal lag between different glomeruli and consistency of dynamics with each sniff. Signals are unfiltered. Lower right shows ITA waveforms for each glomerulus, generated across 137 sniffs over 6 presentations of ethyl butyrate. Vertical line indicates time of inhalation onset.

B. Left: Range of latency to SF-iGluSnFR onset (black) and peak (red) latency, relative to the start of inhalation, measured from ITAs taken from 70 glomerulus-odor pairs (3 fields of view, 2 mice). Left two columns show data compiled across all glomerulus-odor pairs. Notch: median, Box edges: 25th and 75th percentiles, square: mean values, whiskers: standard deviation Right: Spread of latency values seen across all glomeruli imaged in the same field of view (as defined as the difference between maximum (lat_{max}) and minimum (lat_{min}) latencies), for 11 unique odorant-FOVs.

C. Glutamate signals imaged from 4 glomeruli from the same FOV showing responses to each of two odorants, showing distinct temporal response patterns across glomeruli and odorants. Traces are unfiltered and from a single presentation. Top trace shows respiration/sniffing for each trial; vertical dotted lines indicate inhalation peak for reference.

D. SF-iGluSnFR signals imaged from 3 glomeruli, taken from a separate field of view in the same mouse, showing distinct response patterns to a third odorant (3-Octen-2-one). Note weak suppressive response in one glomerulus (top trace).

E. Increasing odorant concentration elicits changes in glutamate signal dynamics in awake mice. Traces show averaged responses (8 presentations) from 4 glomeruli in the same field of view to a low (1:1000 dilution) versus high (1:10) concentration of ethyl tiglate. Note that the response in the most sensitive glomerulus shows increased adaptation at the higher concentration, while other glomeruli show facilitating responses.

F. Changes in glutamate response patterns over the course of odorant presentation, calculated as described for Figure 3. Colored plots show Pearson's r values at successive time-bins for responses to 6 odorants.

Figure 7. Dual-color imaging reveals high correspondence between glutamate and calcium signals in MT cells of the same glomerulus.

A. Post-hoc confocal image showing coexpression of jRGECO1a (magenta) and SF-iGluSnFR.A184S (A184S, green) in MT cells of a Tbet-Cre mouse. Green and magenta arrows indicate membrane and cytoplasmic expression of SF-iGluSnFR and jRGECO, respectively.

B. Dual-color two-photon imaging of A184S and jRGECO signals from MT cells. Left: Mean SF-iGluSnFR fluorescence showing glomerular structure. Middle: odorant-evoked ΔF response maps for SF.iGluSnFR.A184S and jRGECO signals. Note jRGECO signal in dendrites of several MT cells exiting the central glomerulus, with SF-iGluSnFR signal confined to the glomerular neuropil. Right: traces showing time-course of the fluorescence signal in each channel (1 Hz inhalation). Top traces are from glomerular neuropil; lower traces are from dendrites outside of the glomerulus.

C. Odorant-evoked ITA response maps across the green (A184S) and red (jRGECO) channels. Arrows indicate ROIs with traces plotted in (D).

D. ITA traces taken from different glomeruli activated by the odorant in (C), with different onset latencies, times to peak and durations in different glomeruli. Left traces: SF-iGluSnFR.A184S; right traces: jRGECO1a; traces from the same glomerulus are shown with the same color in each set. Each ITA trace is scaled to the same maximum. Vertical lines indicate peak time for the signal in each glomerulus. Note that the relative order of peak times is the same for both signals.

E. Traces showing SF-iGluSnFR and jRGECO signals imaged simultaneously from a glomerulus, with high correspondence between spontaneously-occurring transients. Vertical lines mark transients seen in both signals; downward arrows mark transients seen in the green (A184S) but not red (jRGECO) channels; upward arrows mark transients seen in the red but not the green channel.

Figure 8. High correspondence between odorant-evoked temporal patterns of glutamate signaling and calcium activity in MT cells of the same glomerulus.

A. Left: Mean fluorescence images for SF-iGluSnFR.A184S and jRGECO1a from the same field of view. Right: Traces showing continuous dual-color recording across 11 consecutive odorant presentations, taken from three glomeruli (locations shown in mean fluorescence images at left), showing high correspondence in SF-iGluSnFR.A184S and jRGECO1a signals despite diverse response patterns to different odorants. ROI 3 (lower traces) shows clear suppressive components in both signals. Downward arrows denote a biphasic response in glutamate signal that is not present in the calcium signal.

B. ΔF response maps (left) and trial-averaged SF-iGluSnFR and jRGECO responses (4 presentations) taken from select glomeruli (right), for three odorants, illustrating high correspondence in response dynamics. Same preparation as in (A).

C. Waterfall plots showing time-course of all significantly-responding glomerulus-odor pairs, compiled across 5 fields of view in 3 mice, for SF-iGluSnFR and jRGECO1a signals. Rows are z-scored and scaled to their own maxima, as above. Row order is sorted by the summed response across the odor presentation window. Right: Correlation coefficients of the time-course of the odorant response in each channel (SF-iGluSnFR and jRGECO), shown for every glomerulus-odor pair**.** Correlations are generally high, but are most variable for suppressive responses (blue).

Table 1. List of odorants and concentration used.

Odor Name	Odor Number	Final Estimated ppm (by Experiment Type)					
		ITA	1 Color	2 Color	Awake	Pharm.	Conc. 1x
Butyric acid	1		0.08	0.08			
2-methylbutyric acid	2		0.03	0.03	0.03	0.03	
Valeric acid	3		0.03	0.03			
Hexanoic acid	5	0.2	0.01	0.01	0.01		0.05
Isovaleric acid	6		0.04	0.04		0.04	
2-methylbuteraldehyde	9		2	2			
trans-2-methyl-2-butenal	10		0.7	0.7	0.7	0.7	
Heptanal	11		0.7	0.7			
2-methylvaleraldehyde	13		3	3	3	3	
Ethyl butyrate	19	10				3	2
Vinyl butyrate	20	9	2	2	2	2	3
Methyl valerate	22	8			5	2	2
Ethyl tiglate	22	2			0.6		0.6
Hexyl tiglate	23		1	1	1	1	
s-Methyl thiobutanoate	24		5	5			
Hexyl acetate	25		3	0.3			
Isopropyl tiglate	27		5	5	5	5	
Isoamylacetate	28		1	1			
2-hexanone	29	10			12		3
Menthone	32	0.01					
2-butanone	33		16	16			19
1-Hexanol	40		2	2			
Cyclohexylamine	43		15	15	15	15	
n-Methyl piperidine	45		1	1		1	
2-methoxy-3-methylpyrazine	51			1	1		
2-Isopropyl-3-methoxypyrazine	56		0.2	0.2			
Benzaldehyde	57	0.1					
Methyl benzoate	60	0.3					0.08
Isobutylthiazole	81			0.07	0.07		
3-Octen-2-one	102		4	4			
trans-2-dodecanal	107		0.2				
Furfuyl mercaptan	110		0.7				
Isobutyraldehyde	136		5	5			30

Each row represents a different odorant used in each experimental manipulation. Final Estimated ppm (by Experiment type) is the estimated vapor concentration of each odorant delivered to the animal, estimated from liquid dilution ratios used, reported vapor pressures, and calibration of the odor delivery device used. Odor number represents the internal reference number associated with each odorant, used in Figures 3 and 8.

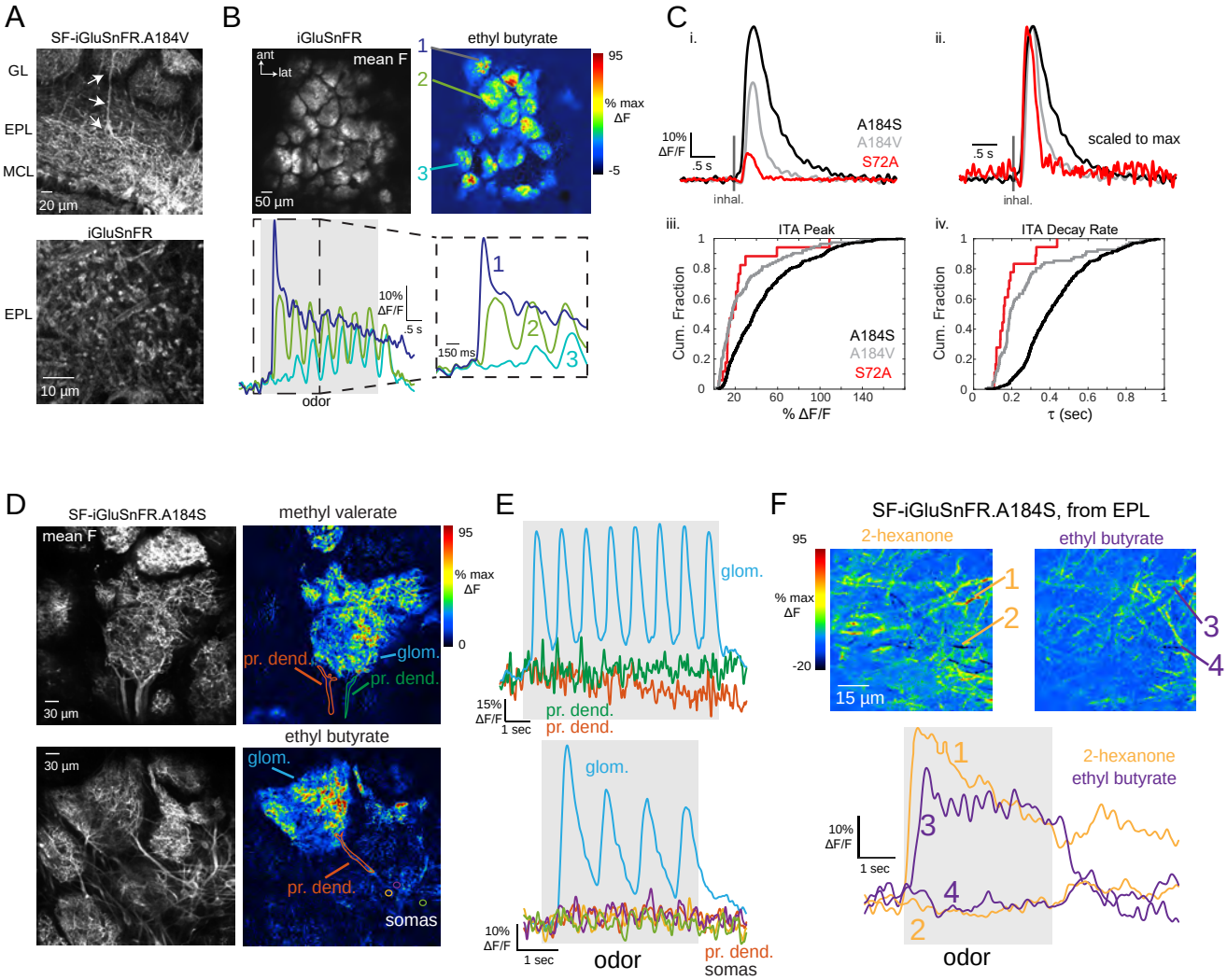

Figure 1. Characterization of iGluSnFRs as reporters of glutamatergic signaling onto MT cells.

A. Expression of iGluSnFR and SF-iGluSnFR in MT cells of the OB.
B. Resting fluorescence, odor repsonse map, and signal time-courses showing odorant-evoked iGluSnFR signal in three glomeruli
C. Comparison of SF-iGluSnFR variants.
D. Subcellular localization of SF-iGluSnFR signals.
E. Responses to odorant taken from the glomerular neuropil, primary dendrite, and MT somata (locations indicated in (D)).
F. Odorant-specific glutamate signals on MT cell lateral dendrites imaged with SF-iGluSnFR.A184S.

Detailed Figure Legends in main text.

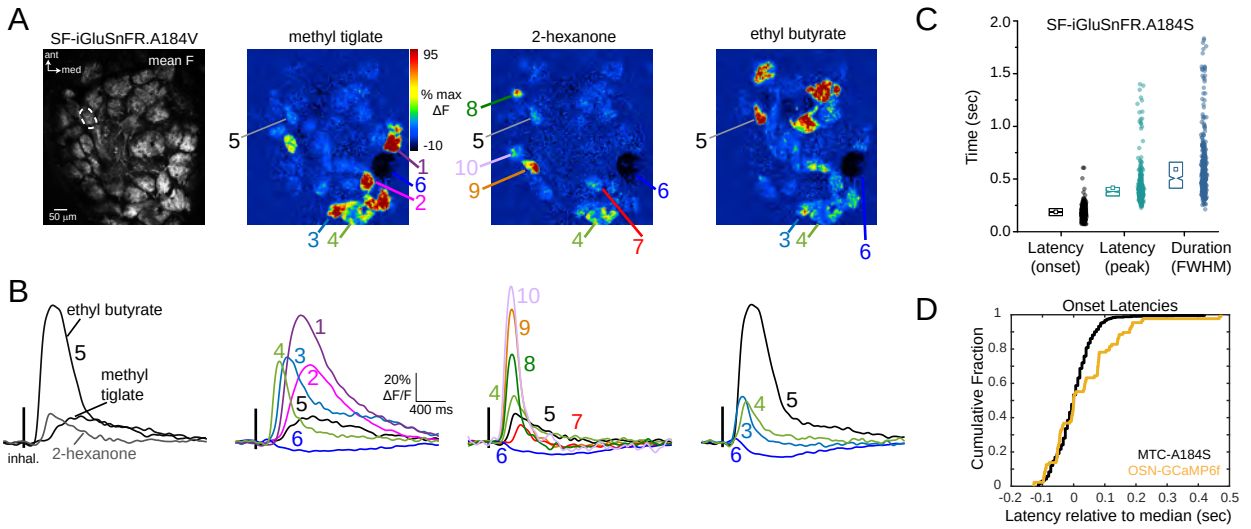

Figure 2. Glomerular glutamate signals show diverse inhalation-driven dynamics.

A. Mean fluorescence image and inhalation-triggered ΔF response maps for three odorants.
B. ITA response traces for the glomeruli indicated in (A).
C. Plot of ITA onset latency, peak latency, and duration (FWHM) for all responsive glomerulus-odor pairs using SF-iGluSnFR.A184S.
D. Cumulative fraction of median-subtracted, ITA onset latencies for SF-iGluSnFR.A184S signals, compared to those measured from GCaMP6f expressed in OSN axon terminals.

Detailed Figure Legends in main text.

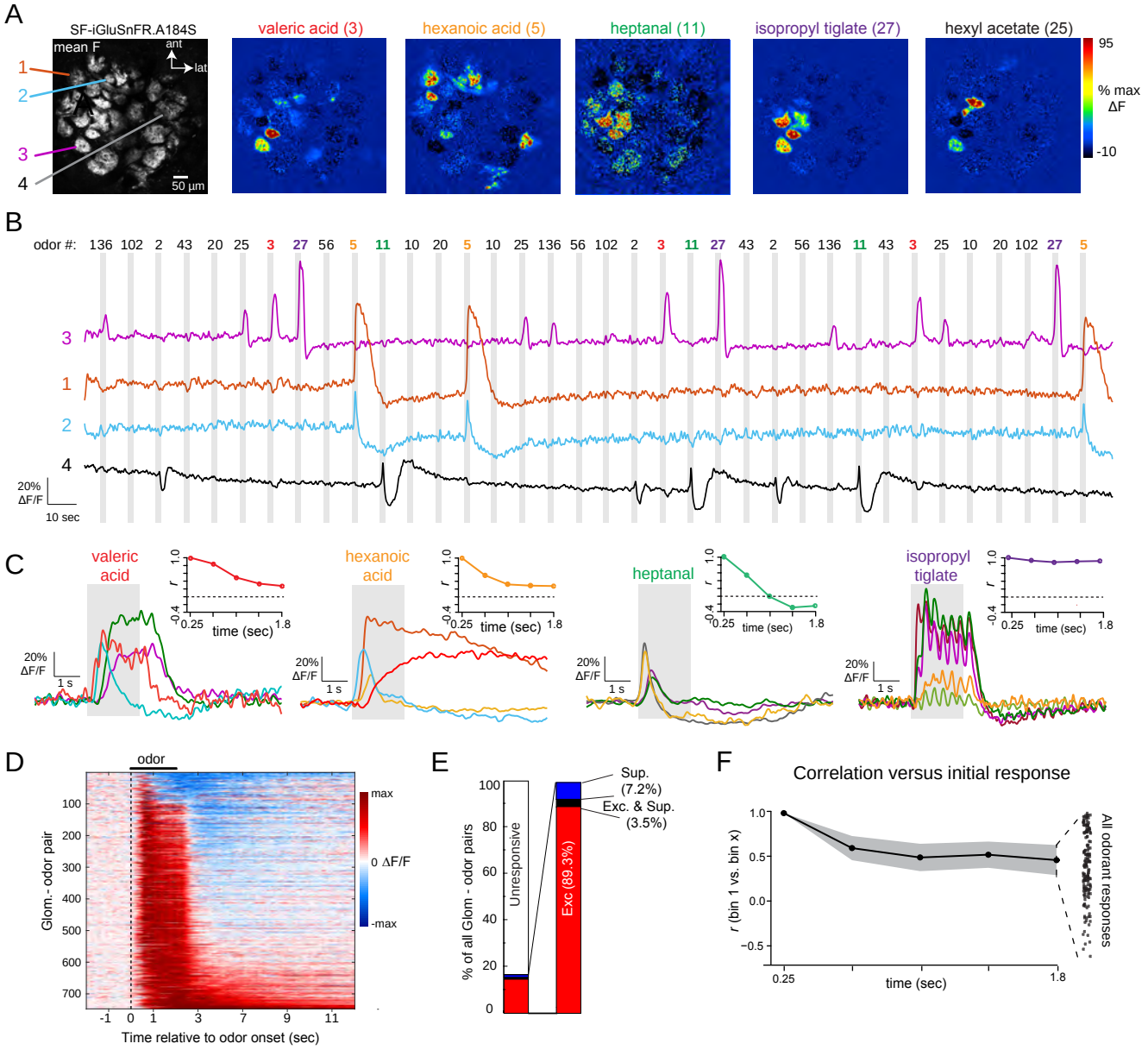

Figure 3. Glomerular glutamate signals show diverse temporal patterns across repeated samples of odorant.

A. Mean fluorescence and ΔF response maps for 5 odorants imaged with SF-iGluSnFR.A184S.

B. Continuous time-series of iGluSnFR signal from 4 glomeruli, over 3 repetitions of 12 odorants.

C. Average response time-course of response in different glomeruli (traces overlaid) to 4 of the 12 odorants. Insets show change in response pattern over the duration of odorant presentation.

D. Time-course of odorant-evoked signal in all significantly-responding glomerulus-odor pairs.

E. Proportion of excitatory, suppressive and biphasic responses across all imaged glomeruli.

F. Change in glutamate response patterns during an odorant presentation, summarized across all odorant presentations. Dots show correlation coefficients at the final time bin for all presentations.

Detailed Figure Legends in main text.

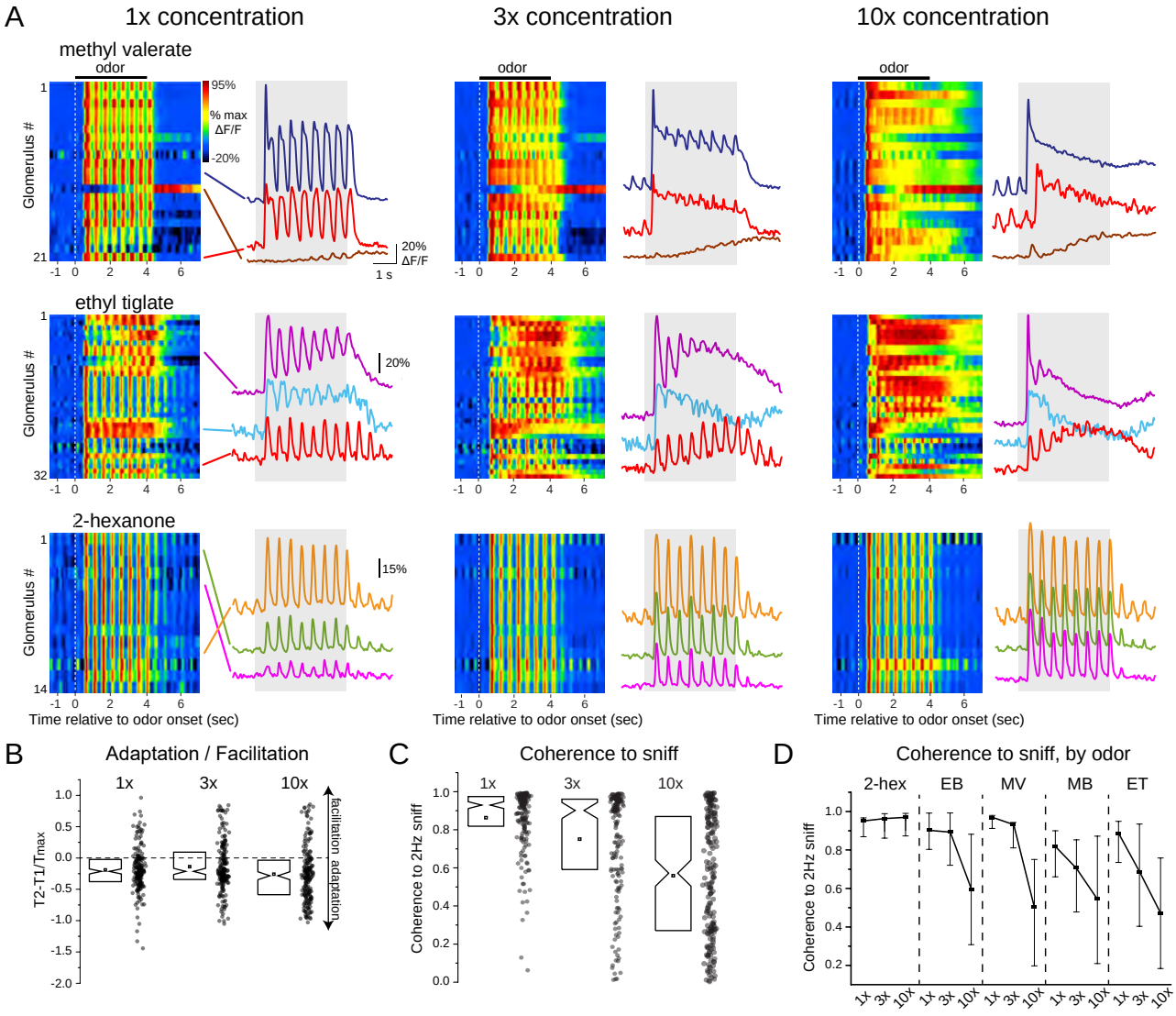

Figure 4. Odorant concentration has systematic impacts on glutamate signaling onto MT cells.

A. Time-courses of iGluSnFR response to 3 concentrations of odorant for three different odorants. All data are from the same experiment and field of view.
B. Summary of adaptation or facilitation of iGluSnFR signal amplitude at each concentration.
C. Coherence of iGluSnFR signal to the 2 Hz inhalation frequency , showing high variability across glomeruli and lower coherence at higher concentration.
D. Coherence values as a function of concentration, plotted separately for each of five odorants.

Detailed Figure Legends in main text.

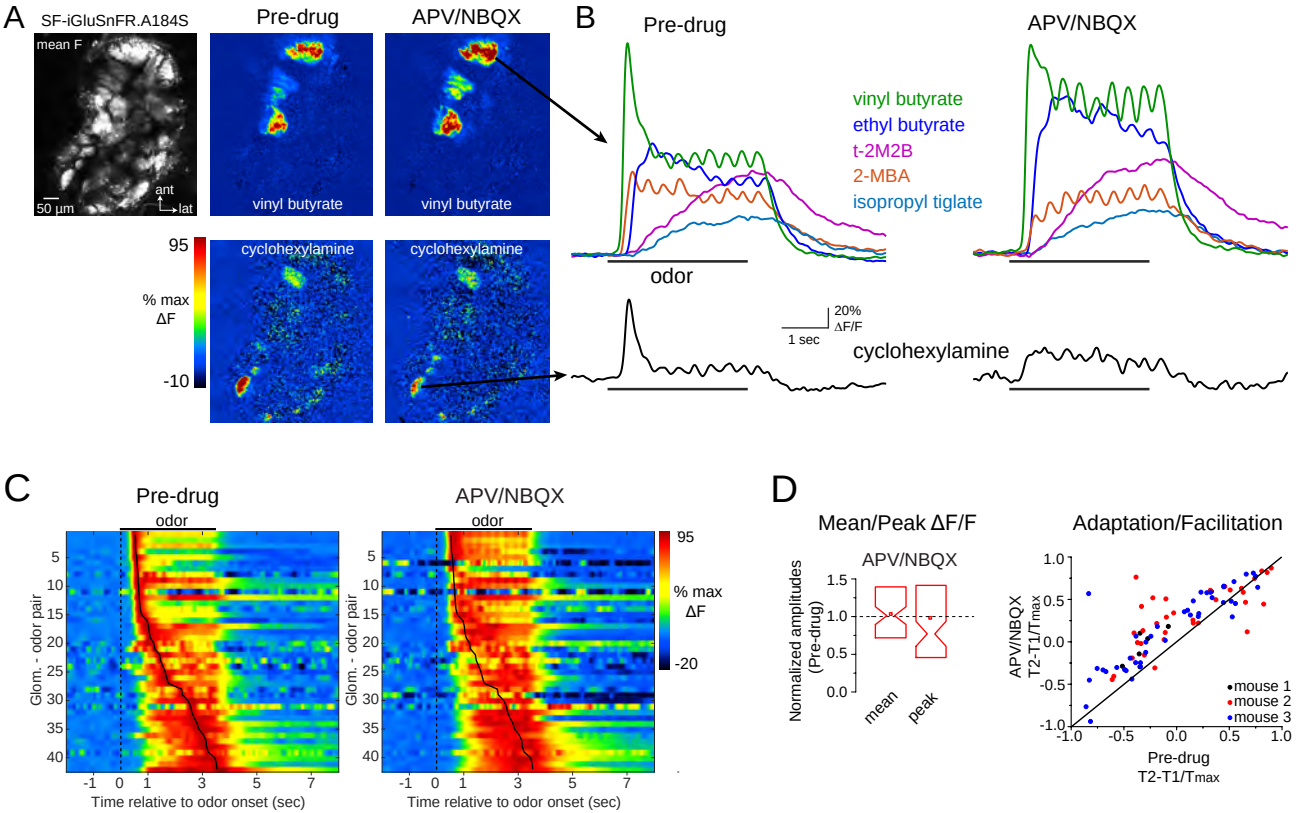

Figure 5. Persistence of diverse glutamate signaling onto MT cells after postsynaptic blockade.

A. Mean fluorescence and odorant response maps (right) for two odorants before and after application of ionotropic receptor blockers (APV/NBQX).

B. Traces of SF-iGluSnFR signal from 2 glomeruli showing that diverse temporal response patterns to different odorants persist after APV/NBQX application, with modest changes to response dynamics.

C. Time-course of all responsive glomerulus-odor pairs in one experiment, before and after application of APV/NBQX.

D. Summary data showing that APV/NBQX does not alter mean or peak odorant responses, but does reduce adaptation in the odorant response when summarized across all glomerulus-odor pairs.

Detailed Figure Legends in main text.

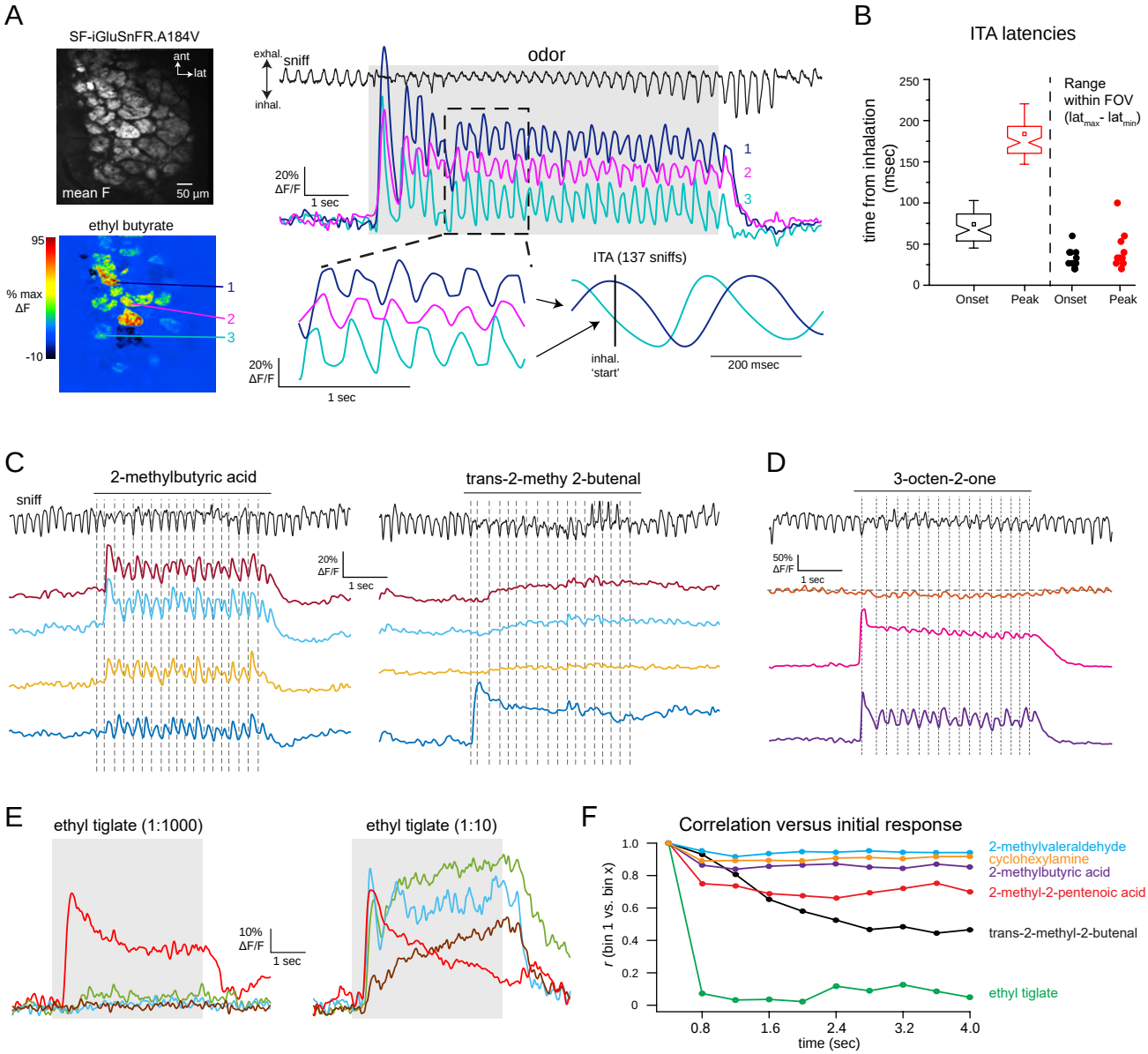

Figure 6. Diversity of glutamate dynamics imaged from MT cells in the awake mouse.

A. SF-iGluSnFR signals imaged from 3 glomeruli in an awake mouse during a single odor presentation, including ITA waveforms for each glomerulus, showing different ITA latencies in different glomeruli.

B. Summary of ITA response latencies across all glomeruli, and range of latencies for glomeruli activated within a given odor response.

C. Traces showing distinct temporal dynamics for different odorants activating the same glomeruli.

D. Traces showing distinct temporal dynamics for different glomeruli activated by the same odorant.

E. Increasing odorant concentration elicits changes in glutamate signal dynamics in awake mice. Each trace is from a different glomerulus imaged in the same field of view.

F. Change in glutamate response patterns over the course of odorant presentation, calculated as described for Figure 3, shown for responses to 6 odorants.

Detailed Figure Legends in main text.

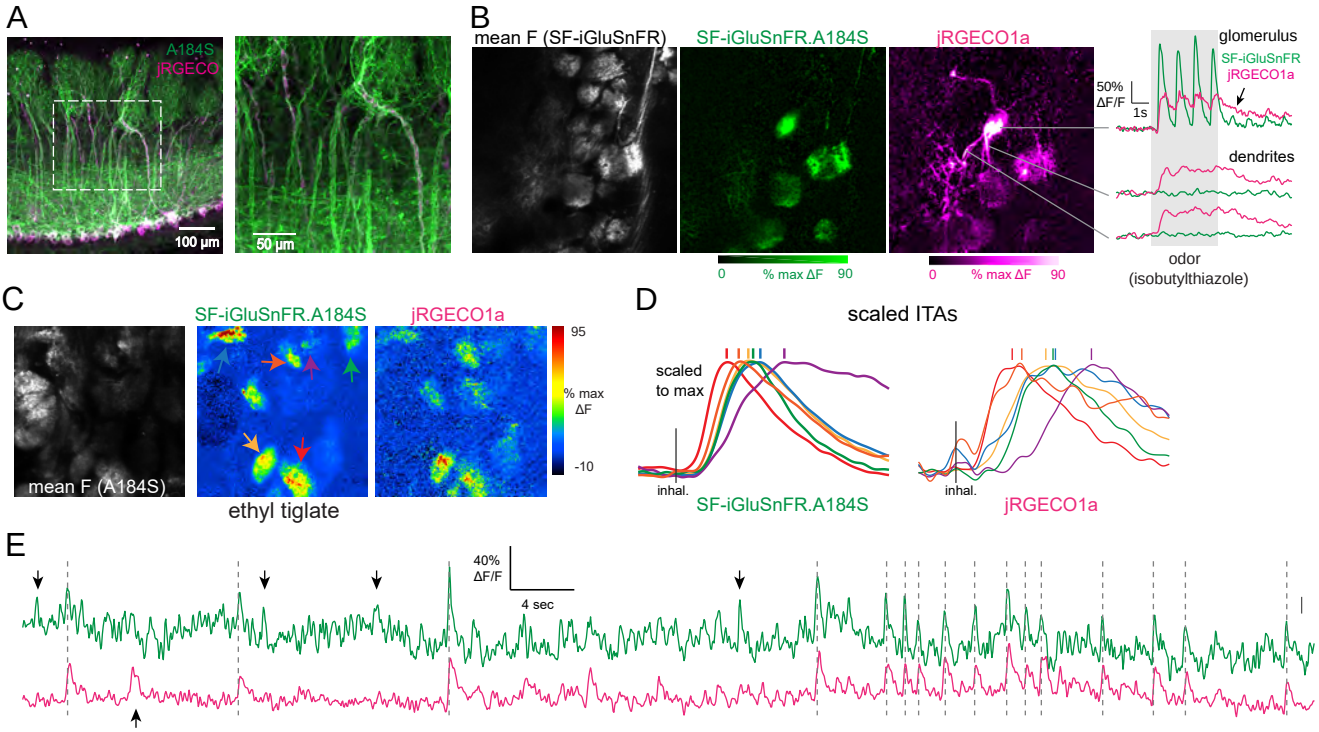

Figure 7. Dual-color imaging reveals high correspondence between glutamate and calcium signals in MT cells of the same glomerulus.

A. Coexpression of jRGECO1a and SF-iGluSnFR.A184S in MT cells of a Tbet-Cre mouse.
B. Dual-color two-photon imaging of glutamate and calcium signals from MT cells.
Left: SF-iGluSnFR fluorescence, showing glomerular structure. Middle: odorant response maps for both signals. Right: time-course of the fluorescence signal in each channel, taken from the glomerulus and from dendrites outside of the glomerulus.
C. Glutamate and calcium odorant response maps, imaged from a different preparation.
D. ITA traces taken from the glomeruli in (C), showing distinct inhalation-linked dynamics across glomeruli, with the relative order of peak times preserved across the glutamate and calcium signals.
E. High correspondence in spontaneously-occurring transients observed in the glutamate and calcium signals, imaged in the absence of odorant activation.

Detailed Figure Legends in main text.

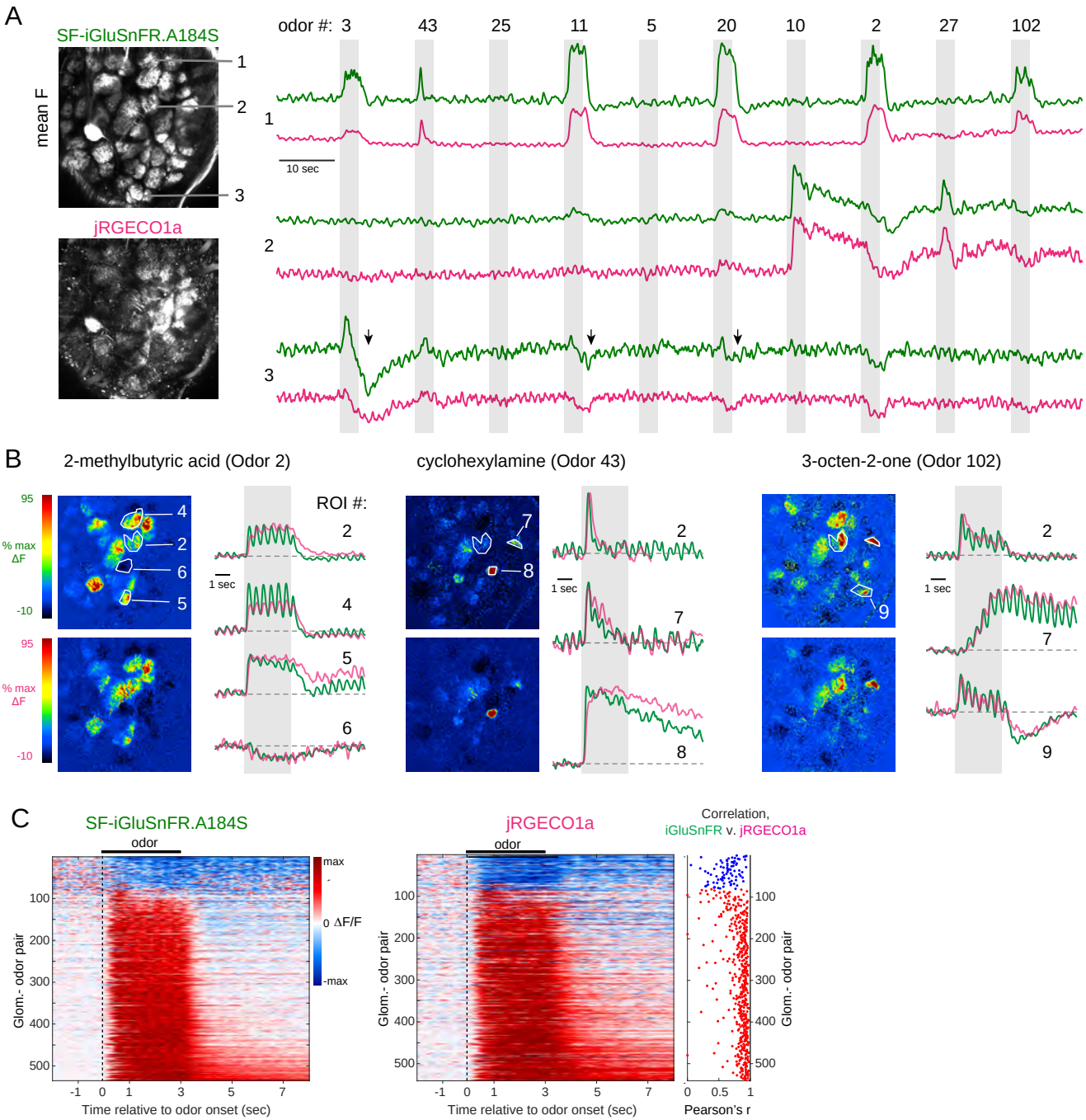

Figure 8. High correspondence between odorant-evoked temporal patterns of glutamate signaling and calcium activity in MT cells of the same glomerulus.

A. Dual-color imaging traces from three glomeruli, showing high correspondence in SF-iGluSnFR and jRGECO1a signals despite diverse responses to different odorants.

B. High correspondence in SF-iGluSnFR and jRGECO response maps and temporal patterns for additional glomeruli. Same preparation as in (A).

C. Correspondence in time-courses of all significantly-responding glomerulus-odor pairs imaged with SF-iGluSnFR and jRGECO1a. Waterfall plots are shown in same row order for each signal. Right plot shows correlation coefficients for the odorant response in each channel.

Detailed Figure Legends in main text.